Central processing of leg proprioception in *Drosophila*

Sweta Agrawal[1], Evyn S Dickinson[1], Anne Sustar[1], Pralaksha Gurung[1], David Shepherd[2], Jim Truman[3,4], John C Tuthill[1*]

[1]Department of Physiology and Biophysics, University of Washington, Seattle, Washington, USA
[2]School of Natural Sciences, Environment Centre Wales, Bangor University, Bangor, Gwynedd, UK
[3]Janelia Research Campus, Howard Hughes Medical Institute, Ashburn, USA
[4]Friday Harbor Laboratories, University of Washington, Friday Harbor, USA
[*]Correspondence and Lead Contact: tuthill@uw.edu

Abstract

Proprioception, the sense of self-movement and position, is mediated by mechanosensory neurons that detect diverse features of body kinematics. Although proprioceptive feedback is crucial for accurate motor control, little is known about how downstream circuits transform limb sensory information to guide motor output. Here, we investigate neural circuits in *Drosophila* that process proprioceptive information from the fly leg. We identify three cell-types from distinct developmental lineages that are positioned to receive input from proprioceptor subtypes encoding tibia position, movement, and vibration. 13Bα neurons encode femur-tibia joint angle and mediate postural changes in tibia position. 9Aα neurons also drive changes in leg posture, but encode a combination of directional movement, high frequency vibration, and joint angle. Activating 10Bα neurons, which encode tibia vibration at specific joint angles, elicits pausing in walking flies. Altogether, our results reveal that central circuits integrate information across proprioceptor subtypes to construct complex sensorimotor representations that mediate diverse behaviors, including reflexive control of limb posture and detection of leg vibration.

Introduction

Mechanosensory neurons provide feedback essential for maintaining stable locomotion through unpredictable environments. A subset of these neurons, the proprioceptors, create an internal representation of body state by monitoring kinematics like joint angles, joint stresses and strains, and muscle length and tension (Proske and Gandevia, 2012). Sensory feedback from proprioceptors contributes to many behaviors, including regulation of body posture (Hasan and Stuart, 1988; Zill et al., 2004), coordination of goal-directed movement (Büschges, 2005; Lam and Pearson, 2002), locomotor adaptation (Bidaye et al., 2017; Dickinson, 2000), and motor learning (Isakov et al., 2016; Takeoka and Arber, 2019).

In both invertebrates and vertebrates, proprioceptors encode diverse features of body kinematics (Brown and Stein, 1966; Lennerstrand, 1968; Tuthill and Azim, 2018). For example, muscle spindles, which are proprioceptive sensory organs embedded in vertebrate skeletal muscles, encode both muscle fiber length and contraction velocity (Hunt, 1990). A functionally analogous structure, the femoral chordotonal organ (FeCO), is housed within the femur of the insect leg (Field and Matheson, 1998) (Fig. 1A). The FeCO is the largest proprioceptive organ in the fruit fly, *Drosophila melanogaster* (Meigen, 1830), and its 152 neurons can be divided into at least three anatomically distinct subtypes: the claw, hook, and club neurons (Mamiya et al., 2018; Maniates-Selvin et al., 2020; Pacureanu et al., 2019; Phillis et al., 1996). Each subtype encodes different kinematic features of the femur-tibia joint: claw neurons encode tibia position (flexion or extension; Fig. 1C), hook neurons encode directional tibia movement (flexion or extension; Fig. 1D), and club neurons encode tibia vibration and bidirectional movement (Fig. 1E). Experimental manipulation of the FeCO in several insect species has revealed its importance during behaviors like walking and targeted reaching (Bässler, 1988; Field and Burrows, 1982; Mendes et al., 2013; Page and Matheson, 2009).

In contrast to the sensory neurons, nothing is known about how proprioceptive signals are combined or transformed by downstream circuits in the *Drosophila* central nervous system. Work in other species has shown that proprioceptors synapse directly onto both motor neurons and complex networks of central neurons in the

vertebrate spinal cord or invertebrate ventral nerve cord (VNC, Burrows, 1996; Proske and Gandevia, 2012). These central neurons play an important role in integrating proprioceptive information across different modalities, muscles, or limbs, and in some cases, integrating proprioceptive information with descending motor commands (Jankowska, 1992; Osseward and Pfaff, 2019; Windhorst, 2007). Ultimately, understanding the role of sensory feedback in motor control will require knowledge about how central neurons transform inputs from limb proprioceptors, as well as their subsequent effect on motor circuits.

Studying the sense of proprioception presents two major challenges. First, proprioception is multimodal: proprioceptors found at the same location in the body can detect different mechanical features produced by self-movement, such as muscle velocity, muscle tension, or joint position (Hasan and Stuart, 1988; Proske and Gandevia, 2012). It is unclear to what degree signals from these diverse proprioceptors are combined to form a composite representation of the body, or whether they are even encoded within a common coordinate system. Additionally, proprioception faces strict constraints on processing speed: in nimble-footed animals like flies, central circuits may have less than 30 ms to process proprioceptive information in between successive steps (DeAngelis et al., 2019). Perhaps as a result, proprioceptive and motor circuits are heavily intermingled: many primary and second-order sensory neurons are also premotor neurons that synapse onto motor neurons (Arber, 2012; Büschges and Gruhn, 2007; Lam and Pearson, 2002). The lack of clear hierarchical structure within the spinal cord and VNC has made it challenging to identify general organizational principles of central proprioceptive processing.

To better understand how central circuits process proprioceptive information, we examined how sensory signals from the fly FeCO are transformed by downstream neurons in the VNC. We first used an anatomical screen to identify three neuronal cell-types positioned to receive input from at least one of the major FeCO subtypes. We then characterized how each cell-type encodes femur-tibia joint kinematics by recording their activity during controlled leg manipulations. Finally, to understand the role of these neurons in motor control, we optogenetically activated each cell-type while tracking fly behavior. Our results reveal that, even at this early stage of sensory processing, information from different FeCO subtypes is combined to form diverse, complex representations of tibia movement and position that underlie a range of behaviors, including postural reflexes and vibration sensing.

Results

The *Drosophila* VNC consists of ~20,000 neurons (Bates et al., 2019) that arise from 30 segmentally-repeated neuroblasts, each of which divides to form an "A" and "B" hemilineage (Truman et al., 2010). Developmental lineages are an effective means to classify neuronal cell-types: neurons within a hemilineage are morphologically similar (Harris et al., 2015; Mark et al., 2019; Truman et al., 2004), express the same transcription factors (Allen et al., 2019; Lacin and Truman, 2016), and release the same primary neurotransmitter (Lacin et al., 2019a). Despite these common features, however, each hemilineage may be composed of many cell-types (Harris et al., 2015; Lacin et al., 2019b), and it remains an open question to what extent neurons within a hemilineage exhibit similar connectivity or function.

We screened a panel of hemilineage-specific split-Gal4 lines for VNC neurons whose dendrites overlap with the axons of FeCO proprioceptors (Fig. 1A). We computationally aligned VNCs with GFP expression in sensory and central neurons (Jefferis et al., 2007) to assess putative connectivity. Based on this analysis, we focused our efforts on three driver lines that label specific central cell-types: (1) a population of GABAergic neurons from the 13B hemilineage (13Bα neurons, Figs. 1F, S1A) that are positioned to receive input from position-tuned claw proprioceptors, (2) a population of GABAergic neurons from the 9A hemilineage (9Aα neurons, Figs. 1G, S1B) that are positioned to receive input from directionally-tuned hook proprioceptors, and (3) a population of cholinergic neurons from the 10Bα hemilineage (Figs. 1H, S1C) that are positioned to receive input from vibration-sensitive club proprioceptors. These three cell-types are not the only central neurons whose dendrites overlap with FeCO axons – however, they were the top three candidates based on light-level anatomy.

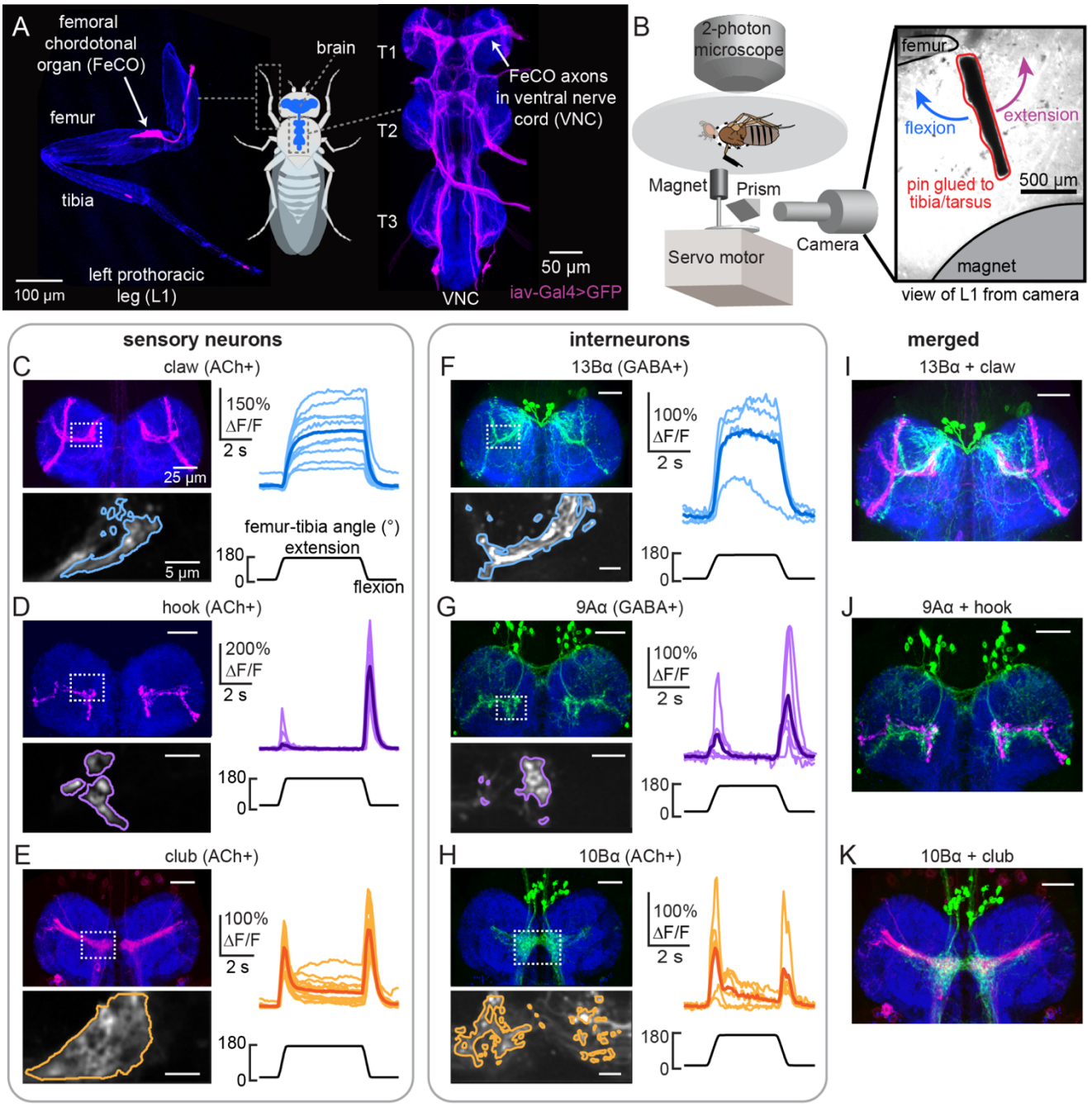

Figure 1. Transformation of leg proprioceptive signals from sensory to central neurons. A) Left: Confocal image of the prothoracic (front) leg showing the location of the femoral chordotonal (FeCO) cell bodies and dendrites (magenta). Blue: cuticle auto-fluorescence. Right: confocal image of FeCO neurons in the fly ventral nerve cord (VNC). Blue: neuropil stain (nc82); Magenta: FeCO axons. B) Experimental set-up for two-photon calcium imaging from VNC neurons while controlling and tracking the femur-tibia joint. A steel pin was glued to the tibia, painted black, and moved via a magnet mounted on a servo motor. The tibia was vibrated by a piezoelectric crystal fixed to the magnet. Right: an example frame from a video used to track joint angle. C-H) Calcium signals from FeCO sensory neurons or central neurons in response to swing movements of the femur-tibia joint. Top left: anatomy (magenta or green) of each cell-type in the prothoracic VNC (blue: nc82). The dashed white box indicates the recording region. Bottom left: GCaMP6f fluorescence within the recording region during an example trial. The pixels comprising each region of interest are outlined. Right: changes in GCaMP6f fluorescence (ΔF/F) during femur-tibia swing movements. The thicker line is the response average (n =10, 13, 14, 4, 6, 6). (I-K) Overlay of sensory axons (magenta) and central neurons (green). Data in C-E were reproduced with permission from Mamiya et al. (2018). All VNC images were aligned using the Computational Morphometry Toolkit (Jefferis et al., 2007).

The anatomy of each cell-type suggests that they receive input from specific leg proprioceptor subtypes. To test this, we expressed the genetically encoded calcium indicator GCaMP6f in each central neuron population. We then recorded calcium activity *in vivo* via two-photon calcium imaging while using a magnetic control system to manipulate the femur-tibia joint (schematized in Fig. 1B, from Mamiya et al., 2018). We applied three classes of mechanical stimuli to the tibia – swing (Fig. 1C-H, S1D, G, and J), ramp-and-hold (Fig. S1E, H, and K), and vibration (Fig. S1F, I, and L).

The calcium responses of each cell-type supported our hypothesis that the different populations of VNC neurons process signals from distinct subtypes of FeCO sensory neurons. Similar to extension-tuned claw neurons, 13Bα neurons tonically increased their calcium activity during tibia extension (Figs. 1C and F, S1D-E) and were not sensitive to tibia vibration (Fig. S1F). Similar to flexion-tuned hook neurons, 9Aα neurons increased their calcium activity during tibial flexion and to a lesser degree during tibial extension (Figs. 1D and G, S1G-H). However, unlike flexion-tuned hook neurons, 9Aα neurons also exhibited large increases in calcium activity during high frequency tibia vibration (Fig. S1I), suggesting they also integrate signals from vibration-sensitive club neurons. Similar to club neurons, 10Bα neurons transiently increased their activity during tibia extension, flexion, and vibration (Figs. 1E and H, S1J-L). Overall, the anatomical proximity and tuning of each cell-type are consistent with the hypothesis that these central neurons encode tibial movement via input from the FeCO.

13Bα neurons linearly encode tibia position via tonic changes in membrane potential

Each of the three cell-types is comprised of multiple neurons per VNC segment. To assess the heterogeneity of encoding within a cell-type, we recorded the activity of single neurons using *in vivo* whole-cell patch clamp electrophysiology (Fig. 2A). Whole-cell recordings also enabled us to resolve faster time-scale dynamics and determine the contribution of inhibitory inputs, providing insight into the transformations that occur between sensory and central neurons.

Whole-cell recordings from individual 13Bα neurons revealed little heterogeneity across cells. All 13Bα cells lacked detectable action potentials (Fig. 2D). As suggested by the population-level calcium imaging, the membrane potential of individual 13Bα cells provides a readout of tibial position: each cell depolarized when the tibia was extended and hyperpolarized when the tibia was flexed (Fig. 2E-F). This response was stereotyped across all cells we recorded from, though there was some cell-to-cell variability in the magnitude of membrane potential fluctuations, perhaps due to variability in recording quality. Upon tibial extension, most cells exhibited a transient increase in membrane potential that then decreased as the tibia was held extended (Fig. 2E). However, even after the tibia was held extended for over 30 seconds, this adaptation was incomplete, and cells maintained a tonic response at steady state.

The response tuning of single 13Bα neurons is similar to population-level tuning of extension-claw sensory neurons (Mamiya et al., 2018). 13Bα activity increased only when the tibia was extended past ~90° (Fig. 2F-G), and the steady-state membrane potential at a given tibia position was greater when the tibia was extended to reach that position than when the tibia was flexed (Fig. 2G). This phenomenon, commonly referred to as hysteresis, could introduce ambiguity for downstream neurons that rely on a representation of absolute leg angle. The degree of hysteresis that we observed (Fig. 2H) is comparable to what has been previously reported for claw neurons (Mamiya et al., 2018).

We used pharmacological manipulations to ask whether the inputs to 13Bα neurons are mediated by chemical or electrical synapses. Bath application of tetrodotoxin (TTX) to the VNC prevents action potential propagation in leg mechanosensory neurons (Tuthill and Wilson, 2016). As expected, TTX abolished activity in 13Bα neurons during tibia movement (Fig. S2A). FeCO sensory neurons release the neurotransmitter acetylcholine (Mamiya et al., 2018), and so we would expect that application of acetylcholine receptor antagonists (methyllycaconitine (MLA), an antagonist of nicotinic receptors, or atropine, an antagonist of muscarinic receptors)

would also block 13Bα activity. Surprisingly, both MLA and atropine had only subtle effects on 13Bα encoding, and never completely abolished 13Bα activity (Fig. S2B-C), suggesting that 13Bα neurons are coupled to claw sensory neurons via electrical synapses. Finally, application of picrotoxin, an antagonist of the inhibitory neurotransmitter receptors, $GABA_a$ and Glu_{Cl}, had no effect on 13Bα activity (Fig. S2D), suggesting that the hyperpolarization during tibia flexion is due to a lack of excitatory input rather than the action of inhibitory interneurons. In summary, 13Bα cells are a relatively homogeneous class of neurons that receive excitatory input from extension-sensitive claw neurons via mixed chemical and electrical synapses.

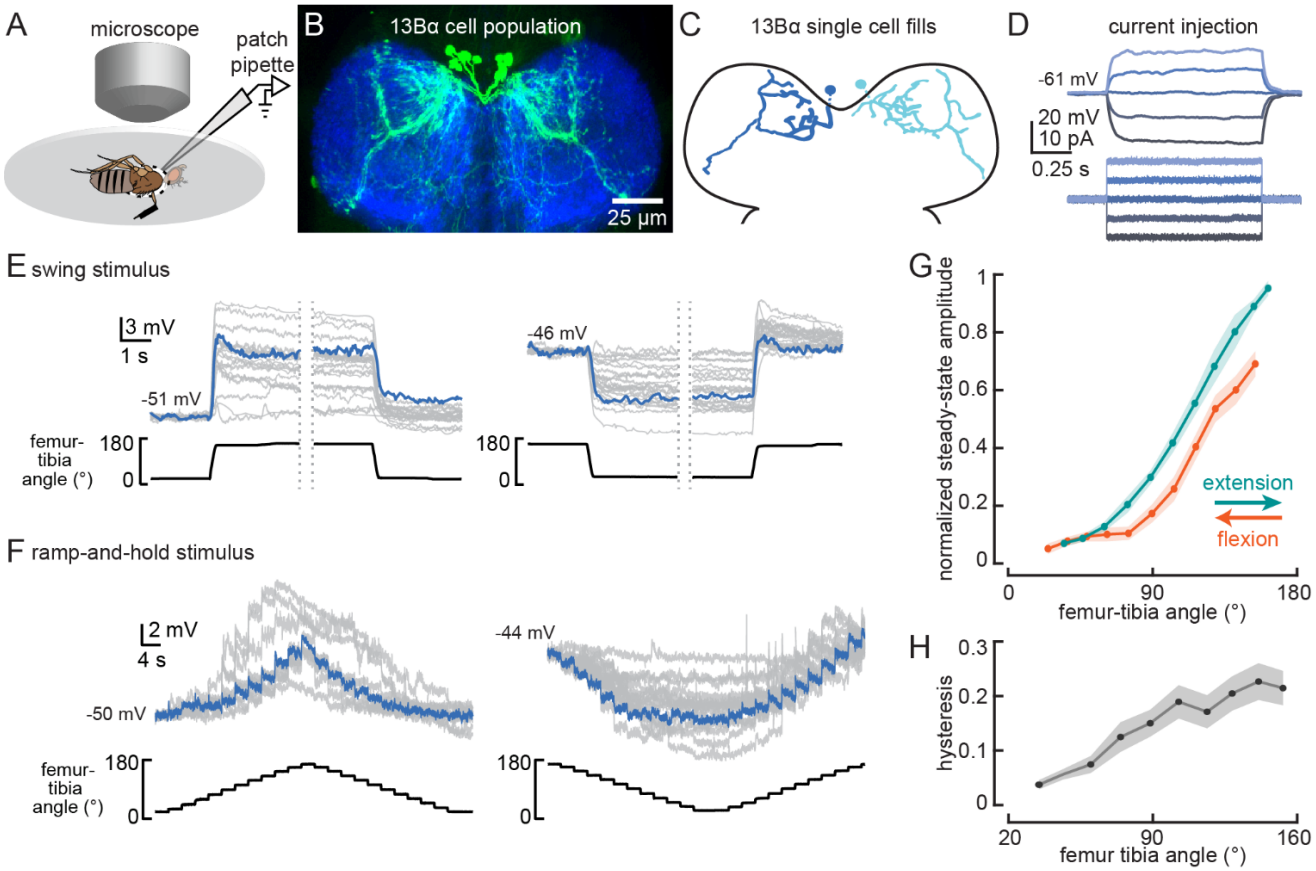

Figure 2. 13Bα neurons encode tibia position via tonic changes in membrane potential. A) The experimental set-up from Fig. 1B was modified for whole-cell electrophysiology. B) Confocal image of 13Bα neurons (green) in the prothoracic VNC. C) Morphology of two 13Bα neurons reconstructed after filling with Neurobiotin. D) Voltage responses to current injection from an example 13Bα recording. E) Whole-cell current clamp recordings during the indicated swings of the femur-tibia joint. Each trace is the average response of a cell to three presentations of the same movement. An example trace is highlighted in blue (left: n = 19; right: n = 23). F) Current clamp recordings during ramp-and-hold movements of the femur-tibia joint. (left: n = 10; right: n = 15) G) Steady-state activity (average +/- SEM) at different joint angles during flexion (orange) or extension (green) from ramp-and-hold trials (tibia began fully flexed). Steady-state responses were measured during the middle second of each 3-second step. Individual traces were normalized to the same maximum amplitude. H) Hysteresis (difference between the response to flexion and extension, average +/- SEM) of the steady-state response plotted in G.

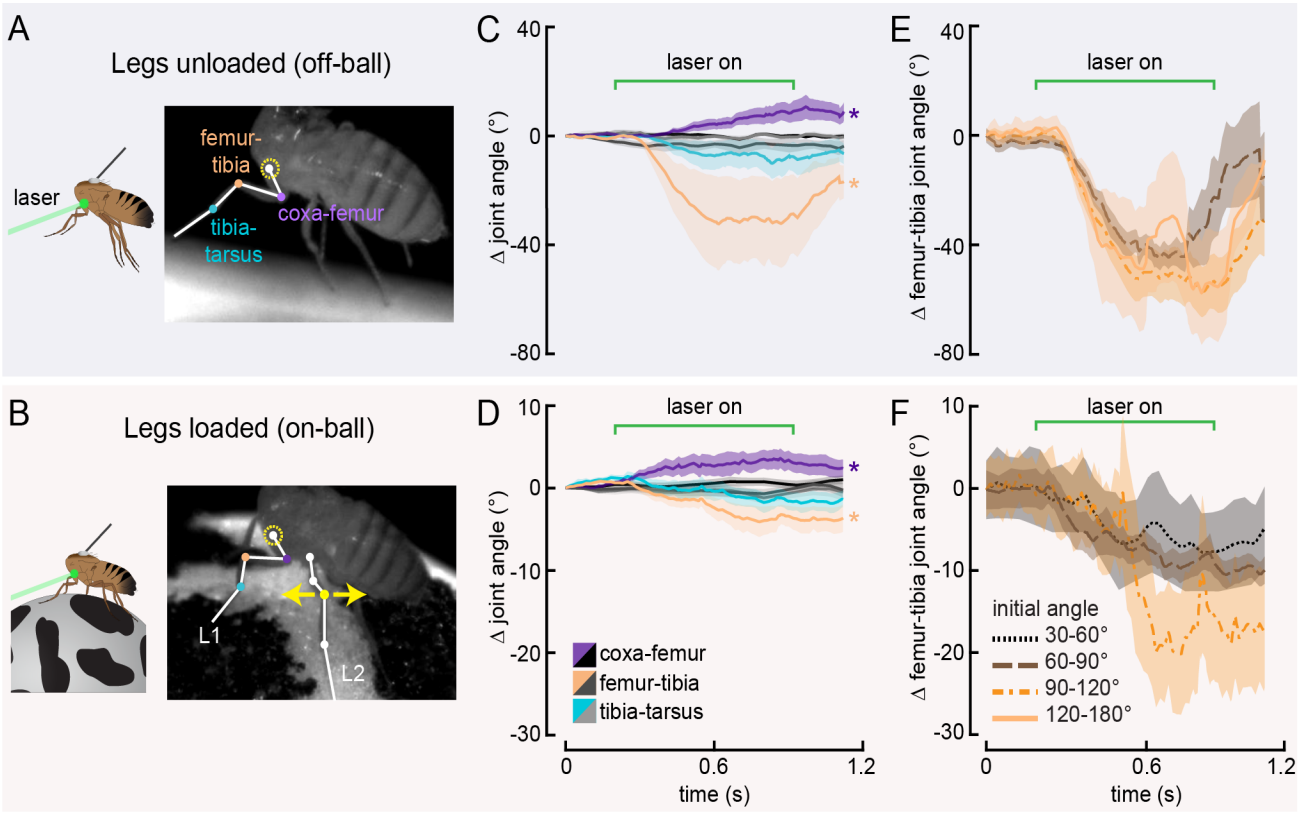

Figure 3. Optogenetic activation of 13Bα neurons causes flexion of the femur-tibia joint. A-B) Schematic (left) and example frame (right) illustrating optogenetic activation of 13Bα neurons in headless flies either suspended from a tether (legs unloaded, A) or positioned on a ball (legs loaded, B). A green laser (530 nm) is focused at the coxa-body joint of the fly's left front leg (outlined in yellow) and the other leg joints are monitored with high-speed video. Yellow arrows illustrate the left middle leg's lateral movements. Top row of panels: legs unloaded; Bottom row: legs loaded. C-D) Average change in joint angle (+/- SEM) of the coxa-femur (purple/black), femur-tibia (orange/dark gray), or tibia-tarsus (blue/light gray). Colored traces are from trials with a 720 ms laser stimulus (as indicated by the green bracket), and the black and gray traces are from trials with no laser stimulus. Asterisks mark those leg joints that demonstrated a significant change in joint angle when the laser was on compared to the no-laser trials (*p<0.05, bootstrapping with false discovery rate correction). Fly is either unloaded (C, n = 4 flies) or loaded (D, n = 7 flies). E-F) Average change in the femur-tibia joint angle during laser stimulation grouped by initial joint angle. Only trials in which the fly flexed the tibia are included. Fly is either unloaded (E, n = 30 trials) or loaded (F, n = 19 trials). None of the groups were significantly different from one another (p<0.05, 1-way ANOVA with Tukey-Kramer correction for comparisons across multiple populations).

Activation of 13Bα neurons causes tibia flexion

Our measurements of 13Bα activity demonstrate that these neurons encode extension of the femur-tibia joint. Their tonic, non-adapting responses suggest a role in encoding, and potentially controlling, posture of the femur-tibia joint. To test this hypothesis, we optogenetically activated 13Bα neurons in tethered, headless flies. We expressed the light-gated cation channel CsChrimson (Klapoetke et al., 2014) in 13Bα neurons and used a green laser focused on the ventral thorax at the base of the left front (L1) leg to activate neurons in the left prothoracic VNC (Fig. 3A-B). Because we were interested in whether these neurons drive reflexive leg movements, we measured how optogenetic activation altered movements of the three major leg joints (coxa-femur, femur-tibia, and tibia-tarsus) in headless flies with their legs unloaded (i.e. the fly was suspended in the air, Fig. 3A) or loaded (i.e. the fly was positioned on a ball, Fig. 3B). In the absence of descending signals from the brain, decapitated flies maintain a consistent leg posture but rarely move their legs spontaneously (Fig. S3A-B). In both loaded and unloaded flies, activation of 13Bα neurons caused a slow extension of the coxa-femur joint and flexion of the femur-tibia joint; this movement was absent during trials without a laser stimulus (Fig. 3C-D, Video S1). During some

trials we also observed a lateral movement of the middle left (L2) leg (Fig. S3A-B, Video S1). The movement of both joints was larger in unloaded flies, whereas the lateral movement of T2 was more likely to occur in loaded flies. For those flies that flexed their femur-tibia joint, the change in joint angle did not vary with initial joint position (Fig. 3E-F). Thus, even though there were systematic differences in the initial joint positions of loaded and unloaded flies (Fig. S3C-D), we hypothesize that the differences we saw between these two conditions is due to the activity of other proprioceptors, such as campaniform sensilla, that are activated by leg loading (Zill et al., 2004). Overall, our results suggest that 13Bα neurons mediate slow postural leg movements in response to limb perturbations detected by the FeCO. Such leg movements are similar to resistance reflexes caused by manipulation of the FeCO in other insects (Field and Matheson, 1998).

9Aα cells exhibit cell-to-cell diversity in their encoding of tibial flexion

The anatomy of 9Aα neurons suggested that they receive input from the directionally tuned hook neurons (Figure 4A-B). Whole-cell recordings confirmed this hypothesis, but also revealed unexpected levels of heterogeneity in the 9Aα population. Each 9Aα cell we recorded from responded to tibia movement through changes in membrane potential and action potential firing rate (Fig. 4C-D). Although individual neurons had consistent tuning across the duration of a recording, each 9Aα cell had slightly different response tuning. The only consistent properties of 9Aα neurons were their directional and speed tuning: subthreshold and spiking activity were largest during fast, flexing swing movements (Figs. 4E-G, S4). Other properties were more variable. For example, some cells were inhibited by tibial extension (Fig. 4E, left), other cells were excited by tibial extension (Fig. 4E, middle and right), and some cells were also tonically depolarized when the tibia was held flexed (Figs. 4E, right, S3B). This latter observation suggests that some 9Aα cells receive direct or indirect inputs from position-sensitive claw neurons. We confirmed that the diversity in 9Aα encoding was not simply due to fly-to-fly variability by recording from two 9Aα neurons in the same fly (Fig. 4H).

Pharmacology experiments revealed that 9Aα cells receive both inhibitory and excitatory inputs. Similar to 13Bα cells, TTX blocked 9Aα encoding of leg movement (Fig. S4C). However, unlike 13Bα cells, MLA also blocked proprioceptive responses in 9Aα neurons (Fig. S4D), indicating that 9Aα activity requires acetylcholine release from FeCO sensory neurons. In all neurons that were hyperpolarized by tibial extension, picrotoxin application abolished the decrease in membrane potential, suggesting that GABAergic inhibition contributes to the encoding of tibial extension (Fig. S4E).

Whole-cell recordings confirmed that 9Aα cells also respond to high frequency tibia vibration (Fig. 5). Because hook neurons are not sensitive to tibia vibration (Mamiya et al., 2018), this observation suggests that 9Aα cells receive direct or indirect input from vibration-sensitive club neurons. Again, we found cell-to-cell heterogeneity in 9Aα vibration encoding. Some cells were inhibited by lower frequency vibration, and as a result, more sharply frequency-tuned (Fig. 5A). Cells also varied in their rates of adaptation: some exhibited a sustained vibration response (Fig. 5B) whereas others adapted quickly after vibration onset (Fig. 5A). Nevertheless, every 9Aα cell was maximally depolarized by 1600-2000 Hz vibrations, and response magnitude increased at higher vibration amplitudes (Fig. 5C). MLA application abolished the vibration response (Fig. 5D). Picrotoxin application abolished inhibitory responses to lower frequency vibration, but also decreased responses to high frequency vibration (Fig. 5E). Thus, in addition to direction-tuned inputs from FeCO hook neurons, 9Aα cells also receive vibration-sensitive inputs from FeCO club neurons.

VNC hemilineages contain multiple cell-types with diverse projection patterns (Harris et al., 2015). Most of our recordings from 9A neurons targeted just one 9A cell-type, the 9Aα cells. However, twice when recording from the driver line labelling 9Aα neurons, we recorded from a cell that was morphologically and physiologically distinct. This cell, which we refer to as 9Aβ, has a cell body located within the same cluster as other 9A neurons, but its neurites extend anteriorly, similar to claw axons (Fig. S5C). 9Aβ cells have larger spikes than 9Aα cells

(>2mV), and they encode flexed tibial positions via tonic changes in membrane potential and firing rate (Fig. S5A-B). 9Aβ cells did not respond to tibial vibration (Fig. S5D), and MLA application mostly blocked their responses to tibia movement (Fig. S5E). This result suggests that the 9A hemilineage broadly integrates sensory input from the FeCO, and different cell-types within the 9A hemilineage receive input from different FeCO sensory neurons.

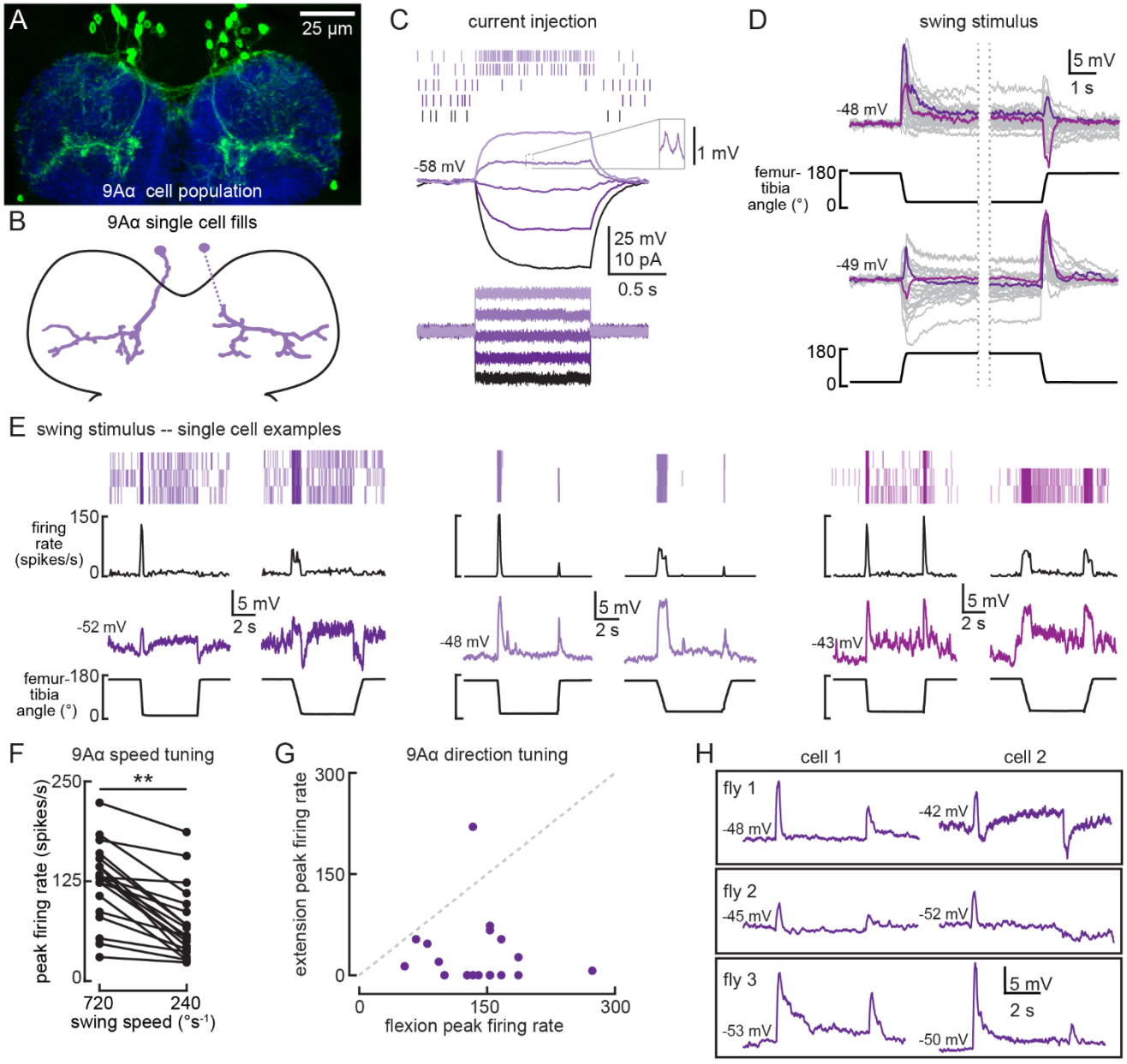

Figure 4. 9Aα neurons are a functionally heterogenous population that encode tibia movement direction. A) Confocal image of 9Aα neurons (green) in the prothoracic VNC. B) Morphology of two 9Aα neurons reconstructed after filling with Neurobiotin. C) Voltage responses to current injection from an example 9Aα recording. Detected spikes are indicated above the voltage traces. Inset shows example spikes, enlarged for clarity. D) Whole-cell current clamp recordings during tibia swing. Each trace is the averaged response to three stimulus presentations. Two example traces are highlighted in purple and magenta (top: n = 35, bottom: n = 27). E) Example whole-cell current clamp recordings from three cells during fast (720°s^{-1}) and slow (240°s^{-1}) swings. Each pair of traces is recorded from a single cell. F) Peak firing rates (averaged across three stimulus presentations) for different flexion speeds (**p<0.005, Wilcoxon matched-pairs signed-rank test). G) For each cell, the peak firing rate when the tibia was flexed relative to when the tibia was extended. Points along the dashed line would represent cells that are equally sensitive to both directions of movement. Points found below the dashed line are tuned for flexion. H) Pairs of 9Aα cells in the same fly have distinct responses to the same 720°s^{-1} swing movement.

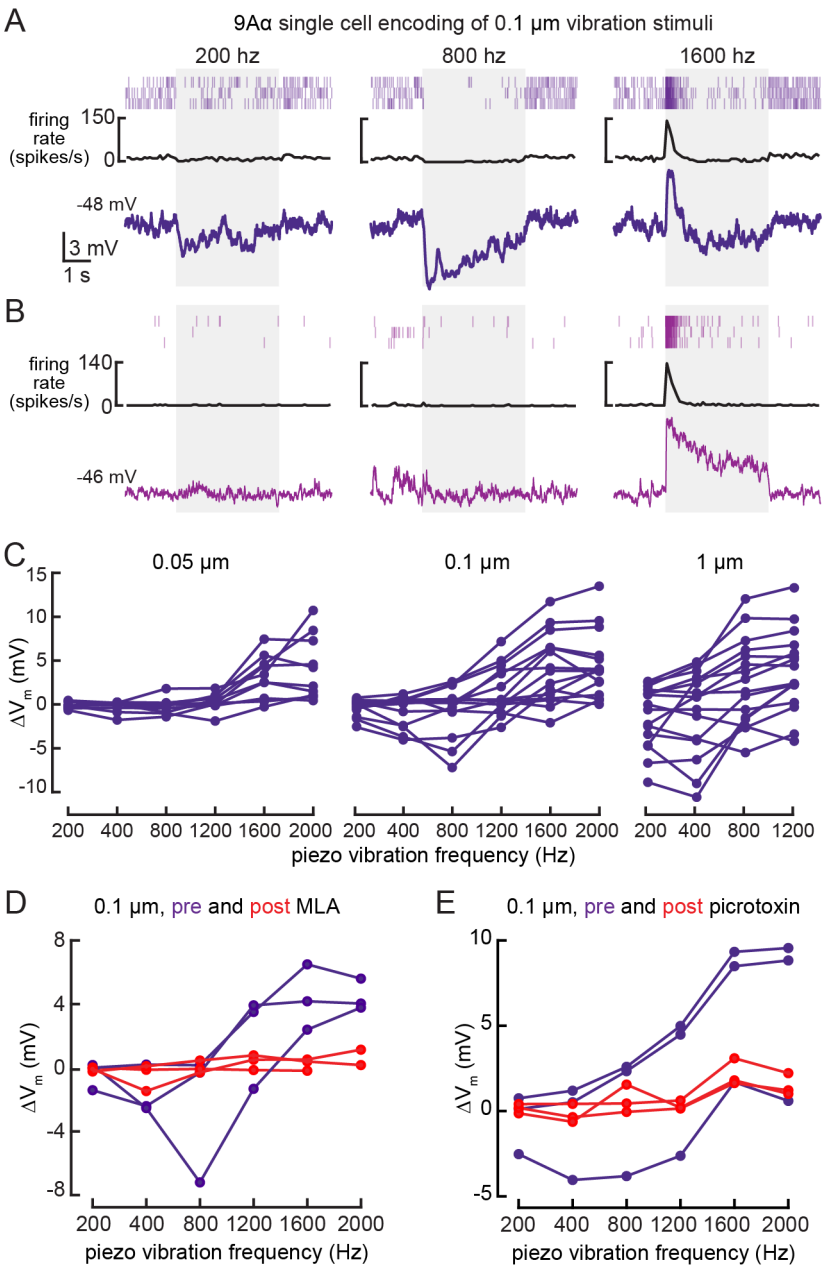

Figure 5. 9Aα neurons encode high frequency tibia vibration. A-B) Example whole-cell current clamp recordings from two 9Aα cells during a 0.1 µm tibia vibration. The shaded region indicates the duration of the vibration stimulus. C) The change in membrane potential during the first 500 ms of vibration across amplitudes and frequencies. Each point is the averaged response of a cell to three stimulus presentations (from left to right, n = 10, 15, 16). D-E) The change in membrane potential during the first 500 ms after vibration onset before (purple) and after (red) application of an antagonist of nicotinic acetylcholine receptors, MLA (1 µM, D), or before (purple) and after (red) application of the $GABA_a$ and GluCl antagonist, picrotoxin (100 µM, E).

Activation of 9Aα neurons causes extension of the tibia-tarsus and femur-tibia joints

Our recordings revealed that 9Aα neurons encode tibia flexion and high-frequency vibration. We next tested if, like 13Bα neurons, optogenetic activation of 9Aα neurons in the left prothoracic VNC (Fig. 6A-B) would cause leg movements in headless flies.

Optogenetic activation of 9Aα neurons produced small extensions of the tibia-tarsus and femur-tibia joints in flies standing on a ball (legs loaded; Figs. 6C-D, Video S2). We observed similar movements in unloaded flies, but they occurred less frequently. We tested a second split-Gal4 line that also labels 9Aα cells (9Aα2-Gal4, Fig. S6), and observed similar extensions of the femur-tibia and tibia-tarsus joints (Fig. S6B-C). Both driver lines may also label one or more 9Aβ cells, meaning we may be activating other 9A cell-types. However, calcium imaging, electrophysiology, and GFP expression all suggest that 9Aα are the predominant cells labeled by both driver lines. As with 13Bα neurons, the differences we saw between loaded and unloaded flies could be due to the activity of other proprioceptors activated by leg loading, or because of systematic differences in initial leg posture (Fig. S6D-E). Compared to the 13Bα neurons, the leg movements caused by 9Aα activation were smaller and more variable. Thus, while both neural populations likely mediate postural adjustments in response to limb perturbations detected by the FeCO, 9Aα neurons may do so in a context-dependent manner, for example to produce small corrective movements during walking.

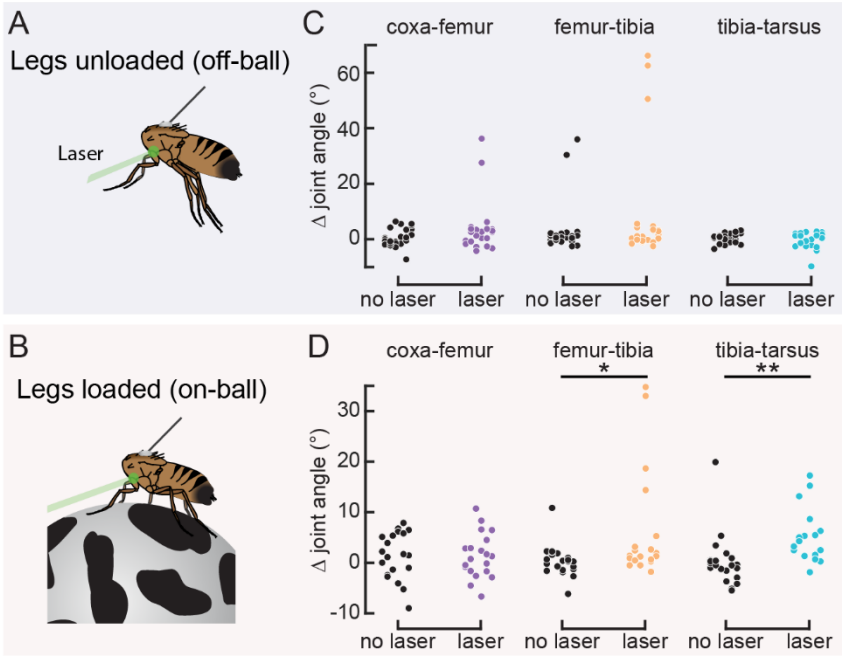

Figure 6. Optogenetic activation of 9Aα neurons causes extension of the tibia-tarsus. A-B) Schematic of optogenetic activation of 9Aα neurons (using 9Aα-Gal4) in headless flies either suspended from a tether (legs unloaded, A) or positioned on a spherical treadmill (legs loaded, B). A green laser (530 nm) is focused at the coxa-body joint of the fly's left front leg. C-D) Change in joint angle after 720 ms during trials in which the laser was on (purple, orange, and blue) or off (black). Each column is data from a single fly. Left: coxa-femur joint; Middle: femur-tibia joint; Right: tibia-tarsus joint. The fly was either unloaded (C, n = 6 flies) or loaded (D, n = 6 flies). (*p<0.05, **p<0.005, bootstrapping with false discovery rate correction).

10Bα neurons integrate information about tibia vibration and position

10Bα neurons are anatomically positioned to receive input from the axons of FeCO club sensory neurons in the VNC (Fig. 7A-B). Each 10Bα neuron innervates multiple VNC segments, and a subset of 10Bα cells project up into the central brain, where they innervate the antennal motor and mechanosensory center (AMMC). We used whole-cell patch-clamp electrophysiology to record the membrane potential of 10Bα neurons with cell bodies in the T1 segment. In our recordings, current injection failed to evoke identifiable action potentials (Fig. 7C), though we did occasionally observe spike-like events. Because these events only occurred in a subset of recordings, we instead analyzed changes in the membrane potential of 10Bα neurons during tibial movements.

Consistent with our hypothesis that 10Bα neurons are downstream of FeCO club neurons, individual cells were transiently depolarized by tibia movements in both directions (Fig. 7D, Fig. S7B-C). Additionally, most 10Bα neurons were tonically hyperpolarized when the tibia was fully flexed and transiently hyperpolarized when the tibia was fully extended (Fig. 7D). Thus, in addition to movement-sensitive excitatory inputs, 10Bα cells also receive position-sensitive inhibition.

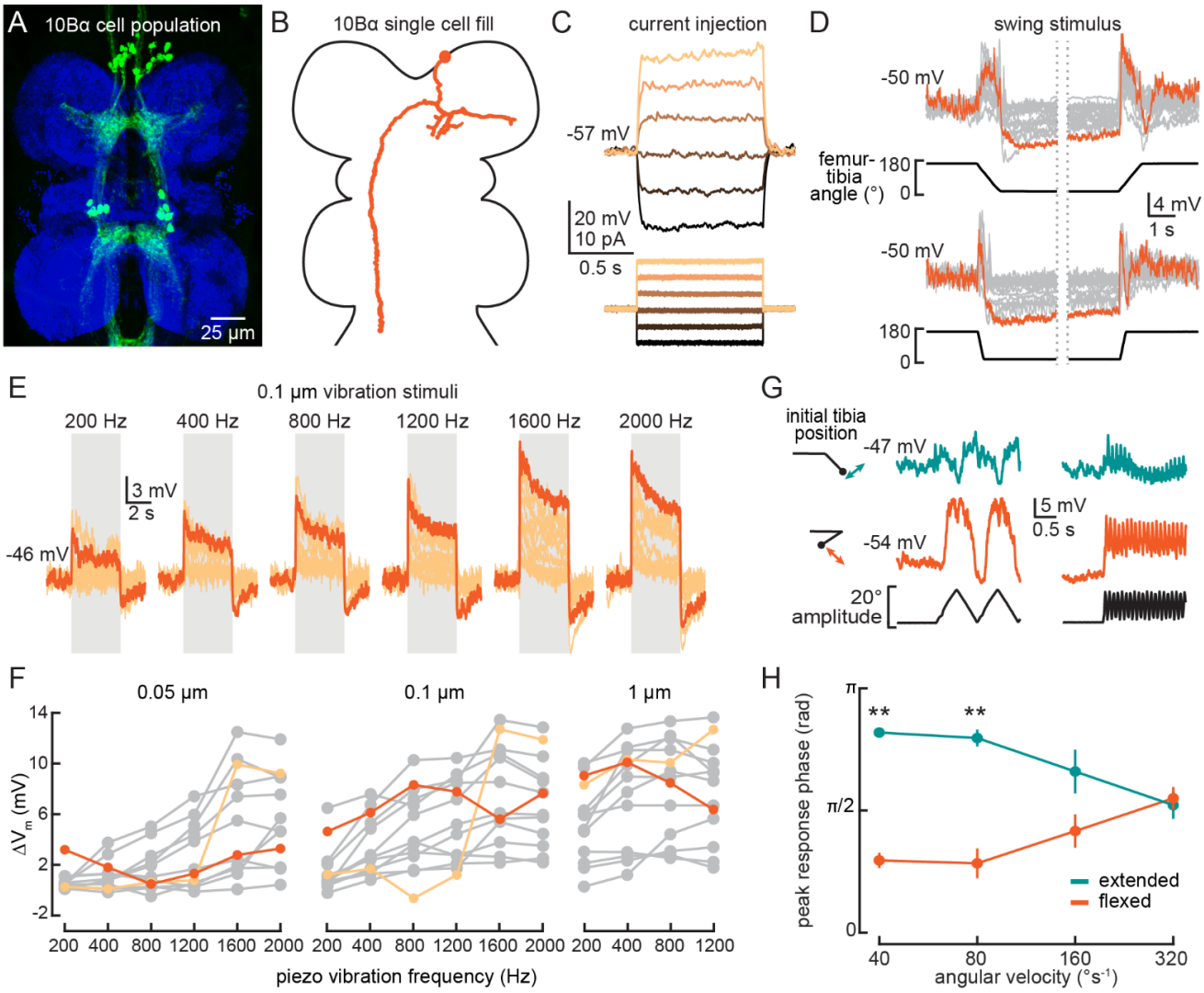

Figure 7. 10Bα neurons encode bidirectional tibia motion and tibia vibration in a position-dependent manner. A) Confocal image of 10Bα neurons (green) in the VNC. B) 10Bα morphology reconstructed after filling with Neurobiotin. C) Voltage responses to current injection from an example recording. D) Whole-cell current clamp recordings during tibia swing movements. Each trace is the average response to three stimulus repetitions. An example trace is highlighted in orange. (top: n = 18, bottom: n = 18) E) Responses to a 0.1 µm vibration stimulus (n = 12 cells). The gray box indicates when the vibration stimulus was applied. An example response is highlighted in dark orange. F) The change in membrane potential during the first 500 ms after vibration onset. Each point is the averaged response to three stimulus repetitions. Two cells with different frequency tuning are highlighted in different shades of orange (left to right, n = 9, 13, 13). G) Example 10Bα recording demonstrating how the responses of a single 10Bα neuron to the same movement stimulus depend on the tibia's position. The tibia began either extended (green) or flexed (orange) and was then oscillated with an amplitude of 20° at four different angular velocities. Responses from the slowest (40°s^{-1}) and fastest (320°s^{-1}) oscillation are shown. H) The phase of the oscillation at which a 10Bα cell is maximally depolarized when the tibia began either flexed (orange) or extended (green) (n = 9, **p<0.005, Wilcoxon matched-pairs signed-rank test).

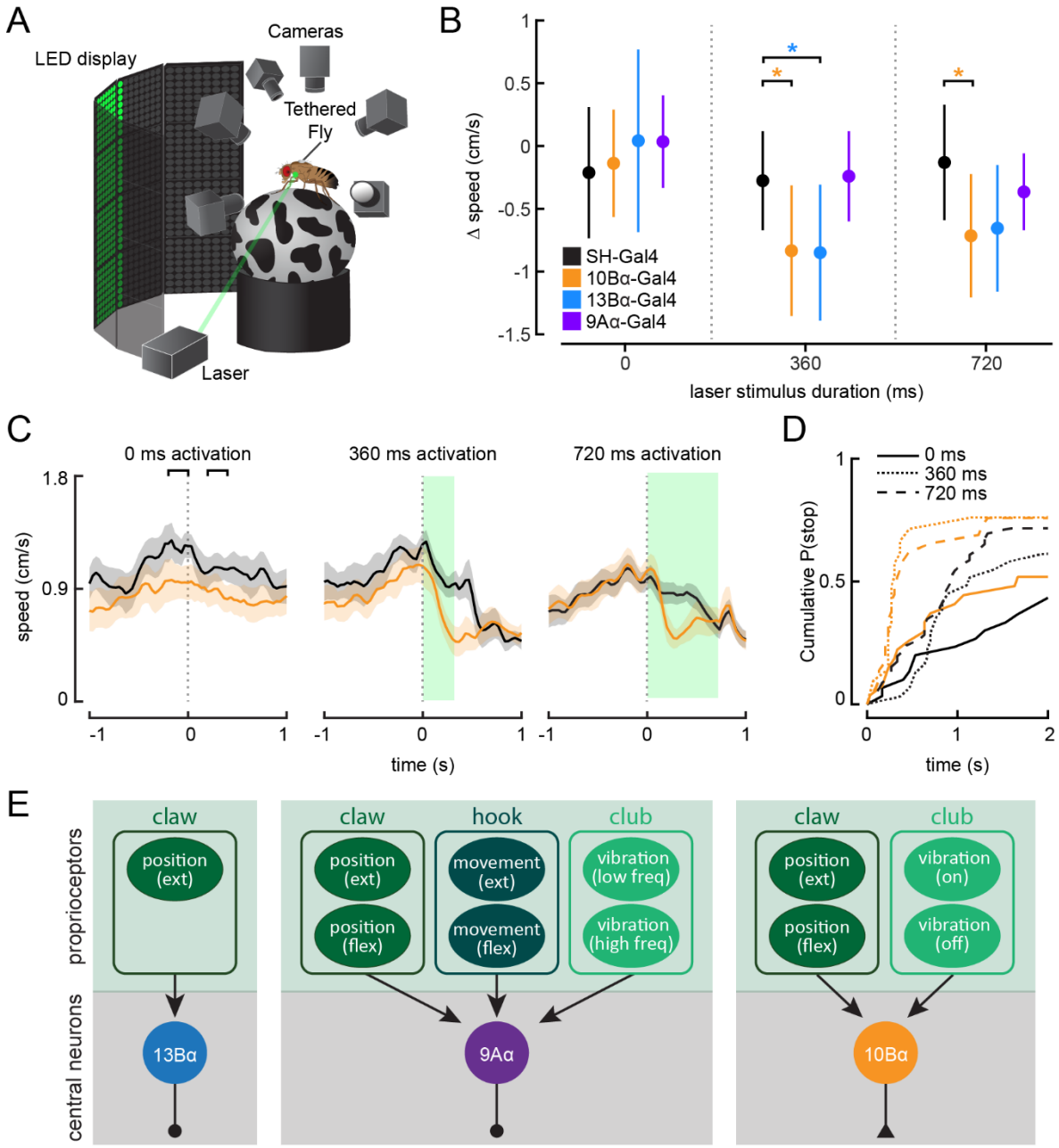

Figure 8. Optogenetic activation of 10Bα neurons causes flies to freeze and stop walking. A) Schematic of optogenetic activation of 10Bα neurons in tethered flies walking on a spherical treadmill. The treadmill and fly are tracked using high-speed cameras, and an LED display plays visual patterns that encourage walking. A green laser (530 nm) is focused on the coxa of the fly's left front leg. B) Difference in speed during the 200 ms preceding the start of the stimulus period compared to a 200 ms window beginning after the start of the stimulus period, as indicated by the brackets in C (*p<0.05, bootstrapping with false discovery rate correction; 0 ms: Control: n = 6 flies; 10Bα: n = 10 flies; 13Bα: n = 7 flies; 9Aα: n = 7 flies; 360 ms: Control: n = 8 flies; 10Bα: n = 10 flies; 13Bα: n = 8 flies; 9Aα: n = 6 flies; 720 ms: Control: n = 13 flies; 10Bα: n = 11 flies; 13Bα: n = 13 flies; 9Aα: n = 11 flies) C) Average treadmill forward velocity (+/- SEM) of walking flies during no laser trials (left) or trials with a 360 ms (middle) or 720 ms (right) laser stimulus. Green boxes indicate the duration of optogenetic stimulation. Black brackets indicate the pre- and post-laser onset time periods used to compare the effect of activation between control and interneuron lines in B. D) Cumulative probability of a fly stopping (velocity <0.3 cm/s) during trials with no laser or trials with a 360 ms or 720 ms laser stimulus (0 ms: Control: 25 trials, 10Bα: 24 trials; 360 ms: Control: 25 trials, 10B: 19 trials; 720 ms: Control: 42 trials, 10Bα: 24 trials). E) Schematic of the three central neuron populations (13Bα, 9Aα, and 10Bα) and their sensory inputs as determined by our experiments.

Like club sensory neurons, we found that 10Bα neurons are sensitive to low amplitude, high frequency vibration of the tibia. Interestingly, different 10Bα cells were tuned to different ranges of vibration frequency (Fig. 7E-F). As vibration amplitude increased, frequency tuning broadened (Fig. 7F, light orange) or shifted (Fig. 7F, dark orange). 10Bα cells are so sensitive that they responded to vibration caused by the saline perfusion system (Fig. S7A, left inset). This perfusion response was absent when the tibia was flexed (Fig. S7A, right inset), suggesting that position-dependent inhibition of 10Bα neurons is sufficient to suppress vibration encoding. Thus, leg position may modulate flies' ability to sense substrate vibration via the FeCO.

Tibia position also modulated the sensitivity and timing of 10Bα activity during larger amplitude movements. When we applied an identical 20° triangle-wave oscillation to the tibia starting at either an extended (~145°) or flexed (~20°) position, tibia position affected both the amplitude and phase of the resulting membrane potential oscillations (Fig. 7G-H). This phase shift decreased as the oscillation frequency increased, and disappeared during movements faster than $320°s^{-1}$. As a result, the effect of tibia position on the timing of 10Bα activity may only be significant during slower movements like grooming or targeted reaching. During faster movements like walking, tibia position will primarily modulate the amplitude of 10Bα activity, not its timing.

Finally, pharmacology experiments suggest that 10Bα neurons, like 13Bα neurons, are electrically coupled to upstream FeCO sensory neurons. Application of acetylcholine antagonists (MLA or atropine) was not sufficient to disrupt 10Bα encoding of tibia swing (Fig. S7E-F) or tibia vibration (Fig. S7H). Application of picrotoxin abolished the tonic hyperpolarization present during tibia flexion for some cells (Fig. S7G), suggesting that 10Bα neurons also receive inhibitory inputs. Application of picrotoxin also decreased responses to vibration and abolished the vibration offset response (Fig. S7I). In summary, 10Bα neurons are intersegmentally projecting central neurons that encode tibia movement and vibration via electrical synapses with club sensory neurons. Their vibration sensitivity is gated by inhibition that depends on the position of the tibia.

10Bα neurons drive pausing behavior in walking flies

10Bα neurons are sensitive to leg movements detected by the FeCO, but optogenetically activating 10Bα neurons in headless flies did not reliably evoke leg movement (data not shown). This result suggests that, unlike 9Aα and 13Bα neurons, 10Bα neurons do not modulate leg postural adjustments.

Behavioral studies of walking flies demonstrate that vibration of the substrate can cause flies to stop walking (Fabre et al., 2012; Howard et al., 2019). To determine if 10Bα neurons could drive this pausing behavior, we optogenetically activated 10Bα neurons in tethered, intact flies walking on a spherical treadmill (Fig. 8A). As with headless flies, we used a green laser focused on the base of the left front leg to activate neurons in the left prothoracic VNC. As an optogenetic control, we used flies that expressed only the Gal4 activation domain but not the DNA-binding domain (SH-Gal4). These flies have a similar genetic background as the split-Gal4 lines labelling the VNC interneurons, but they lack expression of a functional Gal4 protein or CsChrimson. Comparing control flies and CsChrimson-expressing flies allowed us to distinguish behavioral responses that were due to a reaction to the laser (which is within the spectral range of the fly's vision) from those due to optogenetic activation.

Activating 10Bα neurons in walking flies consistently led to flies slowing or stopping after about 200 ms, regardless of the length of the laser stimulus (Figs. 8B-D, S8A, Video S3). Although control flies also sometimes paused during the stimulus period, flies with activated 10Bα neurons paused earlier and more frequently (Fig. 8D). Activating 13Bα also caused flies to slow (Figs. 8B, S8B-C), likely due to movement of the front leg, which interrupted walking. However, despite their vibration sensitivity, activating 9Aα neurons had no effect on flies' walking velocity (Figs. 8B, S8B-C).

Overall, our physiology and behavior data indicate that 10Bα neurons trigger pausing in response to tibia vibration detected by the FeCO. Thus, we propose that vibration-detecting club FeCO neurons and their downstream partners, the 10Bα neurons, may comprise a pathway for sensing external substrate vibration. However, 9Aα

neurons, which drive reflexive leg movements but not pausing, also respond to tibia vibration. This result suggests that encoding of tibia vibration by club neurons contributes to both exteroceptive and proprioceptive mechanosensory processing.

Discussion

The sense of proprioception is mediated by diverse mechanosensory neurons that detect distinct mechanical forces produced by self-movement. In this study, we found that proprioceptive information from these diverse proprioceptors is relayed to VNC neurons that process these signals in parallel (Fig. 8E). Some neurons, like 13Bα, encode only a single kinematic feature, tibia extension, presumably via input from the extension-sensitive claw neurons. In contrast, 9Aα neurons encode a complex combination of tibia movement, high frequency vibration, and flexed joint angles, presumably via inputs from multiple proprioceptor subtypes. 10Bα neurons encode tibia vibration and movement, but this encoding is modulated by position-sensitive inhibitory inputs. These central neurons contribute to a range of behaviors, including postural reflexes and vibration sensing. Overall, our results elucidate some of the neuronal computations that occur in proprioceptive circuits and their importance in leg motor control.

Central integration of proprioceptive sensory information

Similar representations of multiple kinematic features have been described in second-order neurons in other mechanosensory systems. For example, aPN3 neurons, a class of neurons downstream of the Johnston's organ (JO) in the fly antenna, encode antennal vibrations only at specific antennal positions, similar to 10Bα neurons (Chang et al., 2016; Patella and Wilson, 2018). Second-order neurons within the mammalian vestibular nuclei include cells that encode only head-rotational movements (via inputs from the semi-circular canal), only head-translational movements (via inputs from the otolith), or both rotations and translations (Dickman and Angelaki, 2002; Goldberg, 2000). The mixed continuum from unimodal to complex, multimodal encoding is thought to facilitate the vestibular nuclei's role in multiple behaviors, including vestibular-ocular reflexes and disambiguating translational motion from gravitational accelerations (Angelaki and Cullen, 2008; Green and Angelaki, 2010; Green et al., 2005). Similarly, the range of second-order neurons that we found in the VNC are likely shaped by the constraints of processing speed and need for motor flexibility.

Each VNC cell-type we analyzed had a different degree of functional heterogeneity across individual neurons. 9Aα neurons, in particular, demonstrated high cell-to-cell variability in their response tuning. These diverse response profiles may result from different mixtures of inhibitory and excitatory synaptic inputs, similar to what has been observed in aPN3 neurons (Chang et al., 2016). By mixing inhibitory and excitatory inputs in different ratios from different populations of sensory neurons, individual aPN3 neurons demonstrate diverse tuning profiles with sensitivity for different stimulus features. From an information coding perspective, such heterogeneous populations could enable continuous representation of multi-modal stimulus spaces, and encode increased information as a population (Azarfar et al., 2018).

Neural representation of tibia position

Tibia position is encoded by approximately 25 claw sensory neurons, each of which is tuned to a narrow range of femur-tibia joint angles (Mamiya et al., 2018). Claw neurons can be separated into two sub-types encoding either flexed (0-90°) or extended (90-180°) tibia angles. 13Bα neurons, based on their anatomy and activity, are likely downstream of extension-sensitive claw neurons (Figs. 1-2) and the 9Aβ neurons are a complementary population of inhibitory neurons that receive inputs from flexion-sensitive claw neurons (Fig. S4). Unlike movement-encoding 9Aα or 10Bα neurons, these position-encoding central neurons encode information from only a single FeCO subtype, suggesting that movement information is immediately contextualized by position information, whereas

position information can be transmitted independently. Perhaps as a result, optogenetic activation of 13Bα neurons consistently caused leg movements, whereas the effect of 9Aα activation was more variable.

We also found that 13Bα and claw neurons exhibit a similar degree of hysteresis: the steady-state membrane potential at a given tibia position from 90-180° was about 20% greater when the tibia was extended to reach that position than when it was flexed (Fig. 2G). Proprioceptive hysteresis is found in many vertebrate and invertebrate mechanosensory systems (Grigg and Greenspan, 1977; Lennerstrand, 1968; Matheson, 1992; Ridgel et al., 2000). However, it is unclear if hysteresis causes problematic ambiguities for downstream circuits that require an accurate readout of tibia angle, or if it is a useful feature, perhaps compensating for the nonlinear properties of muscle activation in short sensorimotor loops (Zill and Jepson-Innes, 1988). Non-spiking central neurons in locusts (Siegler, 1981a) and stick insects (Büschges, 1990) also exhibit hysteresis, and the effects of hysteresis can be seen in leg motor neuron activity (Field and Burrows, 1982; Siegler, 1981b). These data suggest that hysteresis is preserved within central circuits, and our results show that the same is true in *Drosophila*.

Behavioral function of central proprioceptive neurons

Activating both 13Bα and 9Aα neurons caused flies to move their legs, suggesting that these two populations mediate leg postural reflexes in response to perturbations detected by the FeCO. Such reflexes are important to stabilize posture by maintaining joint position, and work in other insects have shown that they are mediated via pathways between the FeCO and leg motor neurons (Burrows, 1996; Büschges, 1990). Motor neurons controlling the fly tibia are organized according to a gradient of cellular size and electrical excitability that enables motor neurons controlling weak, slow movements to be recruited first, followed by neurons that control progressively stronger, faster movements (Azevedo et al., 2019). We found that 13Bα activation caused generally larger leg movements than 9Aα activation. While this distinction could be due to differences in how strongly we were able to drive the activity of either population, it may also suggest that 13Bα and 9Aα cells may synapse onto motor neurons at different levels of the motor hierarchy. 13Bα neurons could provide input to higher gain intermediate or fast motor neurons whereas 9Aα neurons may synapse onto only the low force, slow motor neurons.

In contrast to 9Aα and 13Bα neurons, activating 10Bα neurons did not produce reflexive leg movements. Instead, 10Bα neurons drive pauses in walking behavior. Previous behavioral experiments found that flies will stop walking when they sense the ground vibrating (Fabre et al., 2012; Howard et al., 2019)—10Bα neurons may mediate this stopping via vibration-sensitive inputs from the FeCO. If true, this would imply that the FeCO functions as both a proprioceptive and exteroceptive organ. This finding is consistent with work in stick insects and locusts that also found that vibration-tuned FeCO neurons do not contribute to postural reflexes (Field and Pflüger, 1989; Kittmann et al., 1996; Stein and Sauer, 1999), and instead mediate startle responses to substrate vibration (Friedel, 1999; Stritih Peljhan and Strauß, 2018; Takanashi et al., 2016). Similar mechanoreceptors that primarily sense substrate vibrations are also found in the limbs of rodents (Prsa et al., 2019).

A subset of 10Bα neurons send ascending projections to the brain, where they innervate the wedge (Fig. S1C), a region that encodes auditory information from the antennae (Patella and Wilson, 2018). These ascending projections raise the possibility that vibration signals from10Bα neurons are integrated with vibration signals from the antennae. Although the purpose of this integration is not entirely clear, one possibility is that leg vibration could sensitize flies to other auditory stimuli. Interestingly, however, vibration encoding by the FeCO is not purely exteroceptive: activating vibration-sensitive 9Aα neurons did not cause walking flies to pause but did cause flies to extend the tibia-tarsus joint. Thus, vibration coding in the FeCO may be used for both exteroceptive detection of substrate vibration and for proprioceptive feedback control of limb movement.

A developmental framework for identifying functional subunits in the insect VNC

In vertebrates, efforts combining knowledge of developmental lineages with physiological techniques have been vital for understanding the function of neurons in the spinal cord (Catela et al., 2015; Jessell, 2000; Lu et al., 2015). We have undertaken a similar approach, beginning with previously developed lineage maps of the anatomy of *Drosophila* VNC neurons (Harris et al., 2015; Shepherd et al., 2016) to identify central neurons that are positioned to receive sensory information from the FeCO. We then built genetic driver lines to label these neurons. Because we still lack quantitative data on the numbers of cells or cell-types within each hemilineage, it is unclear what proportion of a given cell-type is captured by each driver line. Nevertheless, as has been observed in other species (Shepherd and Laurent, 1992; Thompson and Siegler, 1991), we found that neurons from the same hemilineage possess similarities in their neurophysiological properties, encoding of tibial kinematics, and putative connections with upstream FeCO neurons. Thus, knowledge of a cell's developmental origins can be a powerful means to identify functional subunits within the fly VNC.

Drosophila is a holometabolous insect that undergoes metamorphosis, changing from a larva to an adult fly. These two life stages look and behave differently, but their nervous systems are generated by the same segmental array of neuroblasts (Harris et al., 2015; Lacin and Truman, 2016). Neurons arising from the same neuroblast produce a similar set of molecules and innervate similar nerve tracts in both larvae and adults (Birkholz et al., 2015; Lacin and Truman, 2016)—are they also functionally similar? Several central neurons in the larval VNC, such as the Basin neurons, have been implicated in relaying mechanosensory or proprioceptive input to motor circuits (Heckscher et al., 2015; Jovanic et al., 2016; Mark et al., 2019; Ohyama et al., 2015; Zarin et al., 2019). Basin neurons, like adult 9A neurons, descend from lineage 9 and receive inputs from larval chordotonal neurons—do adult 9A neurons also receive nociceptive input or synapse onto motor neurons? Such comparisons will yield insight into how central circuits for proprioception are repurposed following metamorphosis.

Beyond understanding how neural function is conserved across metamorphosis, understanding the relationship between hemilineage identity and circuit function will also reveal how neural circuits are conserved across evolution. Neurons similar to 9Aα or 13Bα neurons have been found in other insects (Burrows, 1996; Büschges, 1990). However, it is difficult to determine whether these populations are homologous based only on their physiology or anatomy. An alternative strategy to assess homology would be to ask whether similar neurons in different insect species arise from homologous neuroblasts. The organization of neuroblasts that gives rise to the insect VNC has undergone little change over 350 million years of insect evolution (Lacin and Truman, 2016; Thomas et al., 1984; Truman and Ball, 1998) and homologous neuroblasts and their resulting lineages have been identified in insects as diverse as silverfish, grasshoppers, and *Drosophila* (Jia and Siegler, 2002; Thomas et al., 1984; Truman and Ball, 1998; Witten and Truman, 1998). Connecting neurons' functions with their developmental origin in different species will yield a powerful system for studying the evolution of sensorimotor circuits, revealing the essential bauplan underlying flexible, fast locomotor control.

Summary

In this study, we identify and describe the physiology, activity, and behavioral function of three populations of central neurons that are positioned to receive direct inputs from proprioceptive sensory neurons. While these cell-types represent only a subset of the neurons that are downstream of the FeCO, they provide valuable insight into how proprioceptive sensory information is integrated by central neurons to influence locomotion and motor control. Already, even at the earliest stages of sensory processing, proprioceptive signals from the FeCO diverge to multiple neuron types with distinct behavioral roles.

What is the significance of the specific representations of femur-tibia joint kinematics encoded by central neurons? Answering this question will ultimately require understanding how the outputs of these neurons feed into motor circuits. *Drosophila* is a uniquely powerful model system for this kind of circuit dissection: recent efforts

have identified and mapped the majority of leg motor neurons (Azevedo et al., 2019; Baek and Mann, 2009; Brierley et al., 2012) and leg sensory neurons (Mamiya et al., 2018; Tsubouchi et al., 2017; Tuthill and Wilson, 2016). Additionally, serial-section EM imaging of the VNC will enable precise reconstructions of the neural connectome (Maniates-Selvin et al., 2020). This solid anatomical framework, coupled with detailed functional investigations of VNC cell-types such as the one undertaken in this study, will deepen our understanding of the fundamental computations underlying proprioception.

Acknowledgements

We thank Haluk Lacin, Anthony Azevedo, and Akira Mamiya for helpful discussions, members of the Tuthill laboratory for feedback on the manuscript, Peter Detweiler, Fred Rieke, and Rachel Wong for generous sharing of equipment, Shellee Cunnington for preparation of solutions, Akira Mamiya, Eric Martinson, and Bryan Venema for technical assistance, and Michael Dickinson for sharing fly stocks. We used stocks obtained from the Bloomington *Drosophila* Stock Center (NIH P40OD018537). We also acknowledge support from the NIH (S10 OD016240) to the Keck Imaging Center at UW, and the assistance of its manager, Nathaniel Peters. ED and PG were partially funded by post-baccalaureate fellowships from the UW Institute for Neuroengineering (UWIN). This work was supported by the UW Royalty Research Fund, a UW Innovation Award, a Searle Scholar Award, a Klingenstein-Simons Fellowship, a Pew Biomedical Scholar Award, a Sloan Research Fellowship, and NIH grant R01NS102333 to JCT.

Author Contributions

SA and JCT conceived the project and designed the experiments. JT and DS identified candidate hemilineages and created the genetic driver lines. SA performed calcium imaging and electrophysiology experiments and analyzed the data. PG and AS performed immunohistochemistry experiments. ED participated in designing behavioral experiments, conducted behavioral experiments, and analyzed the data. SA and JCT wrote the paper with input from the other authors.

References

Allen, A.M., Neville, M.C., Birtles, S., Croset, V., Treiber, C.D., Waddell, S., and Goodwin, S.F. (2019). A single-cell transcriptomic atlas of the adult *Drosophila* ventral nerve cord. BioRxiv 2019.12.20.883884.

Angelaki, D.E., and Cullen, K.E. (2008). Vestibular system: the many facets of a multimodal sense. Annu. Rev. Neurosci. *31*, 125–150.

Arber, S. (2012). Motor Circuits in Action: Specification, Connectivity, and Function. Neuron *74*, 975–989.

Azarfar, A., Calcini, N., Huang, C., Zeldenrust, F., and Celikel, T. (2018). Neural coding: A single neuron's perspective. Neuroscience & Biobehavioral Reviews *94*, 238–247.

Azevedo, A.W., Dickinson, E.S., Gurung, P., Venkatasubramanian, L., Mann, R., and Tuthill, J.C. (2019). A size principle for leg motor control in *Drosophila*. BioRxiv 730218.

Baek, M., and Mann, R.S. (2009). Lineage and Birth Date Specify Motor Neuron Targeting and Dendritic Architecture in Adult *Drosophila*. J. Neurosci. *29*, 6904–6916.

Bässler, U. (1988). Functional Principles of Pattern Generation for Walking Movements of Stick Insect Forelegs: The Role of the Femoral Chordotonal Organ Afferences. Journal of Experimental Biology *136*, 125–147.

Bates, A.S., Janssens, J., Jefferis, G.S., and Aerts, S. (2019). Neuronal cell types in the fly: single-cell anatomy meets single-cell genomics. Current Opinion in Neurobiology *56*, 125–134.

Bidaye, S.S., Bockemühl, T., and Büschges, A. (2017). Six-legged walking in insects: how CPGs, peripheral feedback, and descending signals generate coordinated and adaptive motor rhythms. Journal of Neurophysiology *119*, 459–475.

Birkholz, O., Rickert, C., Nowak, J., Coban, I.C., and Technau, G.M. (2015). Bridging the gap between postembryonic cell lineages and identified embryonic neuroblasts in the ventral nerve cord of *Drosophila melanogaster*. Biology Open *4*, 420–434.

Bogovic, J.A., Otsuna, H., Heinrich, L., Ito, M., Jeter, J., Meissner, G., Nern, A., Colonell, J., Malkesman, O., Ito, K., et al. (2019). An unbiased template of the *Drosophila* brain and ventral nerve cord. BioRxiv 376384.

Brierley, D.J., Rathore, K., VijayRaghavan, K., and Williams, D.W. (2012). Developmental origins and architecture of *Drosophila* leg motoneurons. Journal of Comparative Neurology *520*, 1629–1649.

Brown, M.C., and Stein, R.B. (1966). Quantitative studies on the slowly adapting stretch receptor of the crayfish. Kybernetik *3*, 175–185.

Burrows, Malcolm. (1996). The neurobiology of an insect brain (Oxford: Oxford University Press).

Büschges, A. (1990). Nonspiking Pathways in a Joint-control Loop of the Stick Insect *Carausius Morosus*. Journal of Experimental Biology *151*, 133–160.

Büschges, A. (2005). Sensory Control and Organization of Neural Networks Mediating Coordination of Multisegmental Organs for Locomotion. Journal of Neurophysiology.

Büschges, A., and Gruhn, M. (2007). Mechanosensory Feedback in Walking: From Joint Control to Locomotor Patterns. In Advances in Insect Physiology, J. Casas, and S.J. Simpson, eds. (Academic Press), pp. 193–230.

Catela, C., Shin, M.M., and Dasen, J.S. (2015). Assembly and Function of Spinal Circuits for Motor Control. Annu. Rev. Cell Dev. Biol. *31*, 669–698.

Chang, A.E.B., Vaughan, A.G., and Wilson, R.I. (2016). A Mechanosensory Circuit that Mixes Opponent Channels to Produce Selectivity for Complex Stimulus Features. Neuron *92*, 888–901.

DeAngelis, B.D., Zavatone-Veth, J.A., and Clark, D.A. (2019). The manifold structure of limb coordination in walking *Drosophila*. ELife *8*, e46409.

Dickinson, M.H. (2000). How Animals Move: An Integrative View. Science *288*, 100–106.

Dickman, J.D., and Angelaki, D.E. (2002). Vestibular Convergence Patterns in Vestibular Nuclei Neurons of Alert Primates. Journal of Neurophysiology *88*, 3518–3533.

Euler, T., Hausselt, S.E., Margolis, D.J., Breuninger, T., Castell, X., Detwiler, P.B., and Denk, W. (2009). Eyecup scope—optical recordings of light stimulus-evoked fluorescence signals in the retina. Pflugers Arch - Eur J Physiol *457*, 1393–1414.

Fabre, C.C.G., Hedwig, B., Conduit, G., Lawrence, P.A., Goodwin, S.F., and Casal, J. (2012). Substrate-Borne Vibratory Communication during Courtship in *Drosophila melanogaster*. Curr Biol *22*, 2180–2185.

Field, L.H., and Burrows, M. (1982). Reflex Effects of the Femoral Chordotonal Organ Upon Leg Motor Neurones of the Locust. Journal of Experimental Biology *101*, 265–285.

Field, L.H., and Matheson, T. (1998). Chordotonal Organs of Insects. In Advances in Insect Physiology, P.D. Evans, ed. (Academic Press), pp. 1–228.

Field, L.H., and Pflüger, H.-J. (1989). The femoral chordotonal organ: A bifunctional orthopteran (*Locusta migratori*a) sense organ? Comparative Biochemistry and Physiology Part A: Physiology *93*, 729–743.

Friedel, T. (1999). The vibrational startle response of the desert locust *Schistocerca gregaria*. Journal of Experimental Biology *202*, 2151–2159.

Goldberg, J.M. (2000). Afferent diversity and the organization of central vestibular pathways. Exp Brain Res *130*, 277–297.

Gouwens, N.W., and Wilson, R.I. (2009). Signal Propagation in *Drosophila* Central Neurons. J. Neurosci. *29*, 6239–6249.

Green, A.M., and Angelaki, D.E. (2010). Internal models and neural computation in the vestibular system. Exp Brain Res *200*, 197–222.

Green, A.M., Shaikh, A.G., and Angelaki, D.E. (2005). Sensory vestibular contributions to constructing internal models of self-motion. J. Neural Eng. *2*, S164–S179.

Grigg, P., and Greenspan, B.J. (1977). Response of primate joint afferent neurons to mechanical stimulation of knee joint. Journal of Neurophysiology *40*, 1–8.

Guizar-Sicairos, M., Thurman, S.T., and Fienup, J.R. (2008). Efficient subpixel image registration algorithms. Opt. Lett., OL *33*, 156–158.

Haralick, R.M., and Shapiro, L.G. (1992). Computer and robot vision (Addison-Wesley).

Harris, R.M., Pfeiffer, B.D., Rubin, G.M., and Truman, J.W. (2015). Neuron hemilineages provide the functional ground plan for the *Drosophila* ventral nervous system. ELife *4*, e04493.

Hasan, Z., and Stuart, D.G. (1988). Animal solutions to problems of movement control: the role of proprioceptors. Annu. Rev. Neurosci. *11*, 199–223.

Heckscher, E.S., Zarin, A.A., Faumont, S., Clark, M.Q., Manning, L., Fushiki, A., Schneider-Mizell, C.M., Fetter, R.D., Truman, J.W., Zwart, M.F., et al. (2015). Even-Skipped+ Interneurons Are Core Components of a Sensorimotor Circuit that Maintains Left-Right Symmetric Muscle Contraction Amplitude. Neuron *88*, 314–329.

Howard, C.E., Chen, C.-L., Tabachnik, T., Hormigo, R., Ramdya, P., and Mann, R.S. (2019). Serotonergic Modulation of Walking in *Drosophila*. Current Biology *29*, 4218-4230.e8.

Hunt, C.C. (1990). Mammalian muscle spindle: peripheral mechanisms. Physiological Reviews *70*, 643–663.

Isakov, A., Buchanan, S.M., Sullivan, B., Ramachandran, A., Chapman, J.K.S., Lu, E.S., Mahadevan, L., and Bivort, B. de (2016). Recovery of locomotion after injury in *Drosophila melanogaster* depends on proprioception. Journal of Experimental Biology *219*, 1760–1771.

Jankowska, E. (1992). Interneuronal relay in spinal pathways from proprioceptors. Progress in Neurobiology *38*, 335–378.

Jefferis, G.S.X.E., Potter, C.J., Chan, A.M., Marin, E.C., Rohlfing, T., Maurer, C.R., and Luo, L. (2007). Comprehensive Maps of *Drosophila* Higher Olfactory Centers: Spatially Segregated Fruit and Pheromone Representation. Cell *128*, 1187–1203.

Jenett, A., Rubin, G.M., Ngo, T.-T.B., Shepherd, D., Murphy, C., Dionne, H., Pfeiffer, B.D., Cavallaro, A., Hall, D., Jeter, J., et al. (2012). A GAL4-Driver Line Resource for *Drosophila* Neurobiology. Cell Reports *2*, 991–1001.

Jessell, T.M. (2000). Neuronal specification in the spinal cord: inductive signals and transcriptional codes. Nature Reviews Genetics *1*, 20–29.

Jia, X.X., and Siegler, M.V.S. (2002). Midline lineages in grasshopper produce neuronal siblings with asymmetric expression of Engrailed. Development *129*, 5181–5193.

Jovanic, T., Schneider-Mizell, C.M., Shao, M., Masson, J.-B., Denisov, G., Fetter, R.D., Mensh, B.D., Truman, J.W., Cardona, A., and Zlatic, M. (2016). Competitive Disinhibition Mediates Behavioral Choice and Sequences in *Drosophila*. Cell *167*, 858-870.e19.

Kittmann, R., Schmitz, J., and Büschges, A. (1996). Premotor interneurons in generation of adaptive leg reflexes and voluntary movements in stick insects. Journal of Neurobiology *31*, 512–531.

Klapoetke, N.C., Murata, Y., Kim, S.S., Pulver, S.R., Birdsey-Benson, A., Cho, Y.K., Morimoto, T.K., Chuong, A.S., Carpenter, E.J., Tian, Z., et al. (2014). Independent optical excitation of distinct neural populations. Nature Methods *11*, 338–346.

Lacin, H., and Truman, J.W. (2016). Lineage mapping identifies molecular and architectural similarities between the larval and adult *Drosophila* central nervous system. ELife *5*, e13399.

Lacin, H., Chen, H.-M., Long, X., Singer, R.H., Lee, T., and Truman, J.W. (2019a). Neurotransmitter identity is acquired in a lineage-restricted manner in the *Drosophila* CNS. ELife *8*, e43701.

Lacin, H., Williamson, W.R., Card, G.M., Skeath, J.B., and Truman, J.W. (2019b). Unc-4 acts to promote neuronal identity and development of the take-off circuit in the *Drosophila* CNS. BioRxiv 2019.12.24.887679.

Lam, T., and Pearson, K.G. (2002). The Role of Proprioceptive Feedback in the Regulation and Adaptation of Locomotor Activity. In Sensorimotor Control of Movement and Posture, S.C. Gandevia, U. Proske, and D.G. Stuart, eds. (Boston, MA: Springer US), pp. 343–355.

Lennerstrand, G. (1968). Position and Velocity Sensitivity of Muscle Spindles in the Cat. I. Primary and Secondary Endings Deprived of Fusimotor Activation. Acta Physiologica Scandinavica *73*, 281–299.

Longair, M.H., Baker, D.A., and Armstrong, J.D. (2011). Simple Neurite Tracer: open source software for reconstruction, visualization and analysis of neuronal processes. Bioinformatics *27*, 2453–2454.

Lu, D.C., Niu, T., and Alaynick, W.A. (2015). Molecular and cellular development of spinal cord locomotor circuitry. Front. Mol. Neurosci. *8*.

Mamiya, A., Gurung, P., and Tuthill, J.C. (2018). Neural Coding of Leg Proprioception in *Drosophila*. Neuron *100*, 636-650.e6.

Maniates-Selvin, J.T., Hildebrand, D.G.C., Graham, B.J., Kuan, A.T., Thomas, L.A., Nguyen, T., Buhmann, J., Azevedo, A.W., Shanny, B.L., Funke, J., et al. (2020). Reconstruction of motor control circuits in adult *Drosophila* using automated transmission electron microscopy. BioRxiv 2020.01.10.902478.

Mark, B., Lai, S.-L., Zarin, A.A., Manning, L., Cardona, A., Truman, J.W., and Doe, C.Q. (2019). The role of lineage, hemilineage and temporal identity in establishing neuronal connectivity in the *Drosophila* larval CNS. BioRxiv 617936.

Matheson, T. (1992). Range fractionation in the locust metathoracic femoral chordotonal organ. J Comp Physiol A *170*, 509–520.

Mendes, C.S., Bartos, I., Akay, T., Márka, S., and Mann, R.S. (2013). Quantification of gait parameters in freely walking wild type and sensory deprived *Drosophila melanogaster*. ELife *2*, e00231.

Moore, R.J.D., Taylor, G.J., Paulk, A.C., Pearson, T., van Swinderen, B., and Srinivasan, M.V. (2014). FicTrac: A visual method for tracking spherical motion and generating fictive animal paths. Journal of Neuroscience Methods *225*, 106–119.

Ohyama, T., Schneider-Mizell, C.M., Fetter, R.D., Aleman, J.V., Franconville, R., Rivera-Alba, M., Mensh, B.D., Branson, K.M., Simpson, J.H., Truman, J.W., et al. (2015). A multilevel multimodal circuit enhances action selection in *Drosophila*. Nature *520*, 633–639.

Osseward, P.J., and Pfaff, S.L. (2019). Cell type and circuit modules in the spinal cord. Current Opinion in Neurobiology *56*, 175–184.

Pacureanu, A., Maniates-Selvin, J., Kuan, A.T., Thomas, L.A., Chen, C.-L., Cloetens, P., and Lee, W.-C.A. (2019). Dense neuronal reconstruction through X-ray holographic nano-tomography. BioRxiv 653188.

Page, K.L., and Matheson, T. (2009). Functional Recovery of Aimed Scratching Movements after a Graded Proprioceptive Manipulation. J. Neurosci. *29*, 3897–3907.

Patella, P., and Wilson, R.I. (2018). Functional Maps of Mechanosensory Features in the *Drosophila* Brain. Current Biology *28*, 1189-1203.e5.

Phillis, R., Statton, D., Caruccio, P., and Murphey, R.K. (1996). Mutations in the 8 kDa dynein light chain gene disrupt sensory axon projections in the *Drosophila* imaginal CNS. Development *122*, 2955–2963.

Proske, U., and Gandevia, S.C. (2012). The Proprioceptive Senses: Their Roles in Signaling Body Shape, Body Position and Movement, and Muscle Force. Physiological Reviews *92*, 1651–1697.

Prsa, M., Morandell, K., Cuenu, G., and Huber, D. (2019). Feature-selective encoding of substrate vibrations in the forelimb somatosensory cortex. Nature *567*, 384–388.

Reiser, M.B., and Dickinson, M.H. (2008). A modular display system for insect behavioral neuroscience. J. Neurosci. Methods *167*, 127–139.

Ridgel, A.L., Frazier, S.F., DiCaprio, R.A., and Zill, S.N. (2000). Encoding of forces by cockroach tibial campaniform sensilla: implications in dynamic control of posture and locomotion. Journal of Comparative Physiology A: Sensory, Neural, and Behavioral Physiology *186*, 359–374.

Schindelin, J., Arganda-Carreras, I., Frise, E., Kaynig, V., Longair, M., Pietzsch, T., Preibisch, S., Rueden, C., Saalfeld, S., Schmid, B., et al. (2012). Fiji: an open-source platform for biological-image analysis. Nature Methods *9*, 676–682.

Shepherd, D., and Laurent, G. (1992). Embryonic development of a population of spiking local interneurones in the locust (*Schistocerca gregaria*). Journal of Comparative Neurology *319*, 438–453.

Shepherd, D., Harris, R., Williams, D.W., and Truman, J.W. (2016). Postembryonic lineages of the *Drosophila* ventral nervous system: Neuroglian expression reveals the adult hemilineage associated fiber tracts in the adult thoracic neuromeres. Journal of Comparative Neurology *524*, 2677–2695.

Siegler, M.V. (1981a). Posture and history of movement determine membrane potential and synaptic events in nonspiking interneurons and motor neurons of the locust. Journal of Neurophysiology *46*, 296–309.

Siegler, M.V. (1981b). Postural changes alter synaptic interactions between nonspiking interneurons and motor neurons of the locust. Journal of Neurophysiology *46*, 310–323.

Stein, W., and Sauer, A.E. (1999). Physiology of vibration-sensitive afferents in the femoral chordotonal organ of the stick insect. J Comp Physiol A *184*, 253–263.

Stritih Peljhan, N., and Strauß, J. (2018). The mechanical leg response to vibration stimuli in cave crickets and implications for vibrosensory organ functions. J Comp Physiol A *204*, 687–702.

Takanashi, T., Fukaya, M., Nakamuta, K., Skals, N., and Nishino, H. (2016). Substrate vibrations mediate behavioral responses via femoral chordotonal organs in a cerambycid beetle. Zoological Letters *2*, 18.

Takeoka, A., and Arber, S. (2019). Functional Local Proprioceptive Feedback Circuits Initiate and Maintain Locomotor Recovery after Spinal Cord Injury. Cell Reports *27*, 71-85.e3.

Thomas, J.B., Bastiani, M.J., Bate, M., and Goodman, C.S. (1984). From grasshopper to *Drosophila* : a common plan for neuronal development. Nature *310*, 203–207.

Thompson, K.J., and Siegler, M.V.S. (1991). Anatomy and physiology of spiking local and intersegmental interneurons in the median neuroblast lineage of the grasshopper. Journal of Comparative Neurology *305*, 659–675.

Truman, J.W., and Ball, E.E. (1998). Patterns of embryonic neurogenesis in a primitive wingless insect, the silverfish, *Ctenolepisma longicaudata*: comparison with those seen in flying insects. Dev Gene Evol *208*, 357–368.

Truman, J.W., Schuppe, H., Shepherd, D., and Williams, D.W. (2004). Developmental architecture of adult-specific lineages in the ventral CNS of *Drosophila*. Development *131*, 5167–5184.

Truman, J.W., Moats, W., Altman, J., Marin, E.C., and Williams, D.W. (2010). Role of Notch signaling in establishing the hemilineages of secondary neurons in *Drosophila melanogaster*. Development *137*, 53–61.

Tsubouchi, A., Yano, T., Yokoyama, T.K., Murtin, C., Otsuna, H., and Ito, K. (2017). Topological and modality-specific representation of somatosensory information in the fly brain. Science *358*, 615–623.

Tuthill, J.C., and Azim, E. (2018). Proprioception. Current Biology *28*, R194–R203.

Tuthill, J.C., and Wilson, R.I. (2016). Parallel Transformation of Tactile Signals in Central Circuits of *Drosophila*. Cell *164*, 1046–1059.

Windhorst, U. (2007). Muscle proprioceptive feedback and spinal networks. Brain Research Bulletin *73*, 155–202.

Witten, J.L., and Truman, J.W. (1998). Distribution of GABA-like immunoreactive neurons in insects suggests lineage homology. Journal of Comparative Neurology *398*, 515–528.

Zarin, A.A., Mark, B., Cardona, A., Litwin-Kumar, A., and Doe, C.Q. (2019). A *Drosophila* larval premotor/motor neuron connectome generating two behaviors via distinct spatio-temporal muscle activity. BioRxiv 617977.

Zill, S.N., and Jepson-Innes, K. (1988). Evolutionary adaptation of a reflex system: sensory hysteresis counters muscle 'catch' tension. J. Comp. Physiol. *164*, 43–48.

Zill, S., Schmitz, J., and Büschges, A. (2004). Load sensing and control of posture and locomotion. Arthropod Structure & Development *33*, 273–286.

Methods

Fly husbandry

Drosophila were raised on cornmeal agar food on a 14h dark/10h light cycle at 25°C. Females flies, 1-3 days post eclosion, were used for all electrophysiology experiments. Female flies, 4-8 days post eclosion, were used for all *in vivo* calcium imaging experiments. For tethered behavior experiments, both male and female flies, between 2-10 days post-eclosion, were used. For experiments involving optogenetic reagents (CsChrimson), adult flies were placed on cornmeal agar with all-trans-retinal (35mM in 95% EtOH, Santa Cruz Biotechnology) for 24 hrs prior to the experiment. Vials were wrapped in foil to reduce optogenetic activation during development.

Fly preparation for *in vivo* two-photon calcium imaging or electrophysiology

To gain optical access to the VNC while moving the tibia, we used one of two previously described fly holders: for calcium imaging experiments, we used the holder as described by Mamiya et al. (2018), whereas for electrophysiology experiments, we used the holder as described by Tuthill and Wilson (2016) (Figure 1B). Flies were anesthetized on ice and then positioned ventral side up, with the head glued to the upper side of the fly holder using UV-cured glue (Bondic or Kemxert 300). We further glued the ventral side of the thorax onto the hole and on the bottom side of the holder, we glued down the femur of the experimental leg (the right prothoracic leg for the majority of experiments, unless otherwise indicated) so that we could control the femur-tibia joint angle by moving the tibia. When gluing the femur, we held it at a position where the movement of the tibia during the rotation of the femur-tibia joint was parallel to the plane of the fly holder. To eliminate mechanical interference, we glued down all other legs. We also pushed the abdomen to the left side and glued it at that position, so that the abdomen did not block tibia flexion. To position the tibia using the magnetic control system described below, we cut a small piece of insect pin (length ~1.0 mm, 0.1 mm diameter; Living Systems Instrumentation) and glued it onto the tibia and the tarsus of the right prothoracic leg. To enhance contrast and improve tracking of the tibia/pin position, we painted the pin with either black India ink (for calcium imaging experiments, Super Black, Speedball Art Products) or white acrylic paint (for electrophysiology experiments, Liquitex heavy body acrylic, titanium white). After immersing the ventral side of the preparation in extracellular fly saline (recipe below), we removed the cuticle above the prothoracic segment of the VNC and took out the digestive tract to reduce the movements of the VNC. We also removed fat bodies and larger trachea to improve access to the leg neuropil. The perineural sheath under the hole was removed for electrophysiological recordings but left intact for calcium imaging. Fly saline contained: 103 mM NaCl, 3 mM KCl, 5 mM TES, 8 mM trehalose, 10 mM glucose, 26 mM NaHCO3, 1 mM NaH2PO4, 1.5 mM CaCl2, and 4 mM MgCl2 (pH 7.1, osmolality adjusted to 270-275 mOsm). Recordings were performed at room temperature.

Image acquisition using a two-photon excitation microscope

We used a modified version of a custom two-photon microscope previously described in detail (Euler et al., 2009). For the excitation source, we used a mode-locked Ti/sapphire laser (Mira 900-F, Coherent) set at 930 nm and adjusted the laser power using a neutral density filter to keep the power at the back aperture of the objective (40x, 0.8 NA, 2.0 mm wd; Nikon Instruments) below ~25 mW during the experiment. We controlled the galvo laser scanning mirrors and the image acquisition using ScanImage software (version 5.2) within MATLAB (MathWorks). To detect GCaMP6f and tdTomato fluorescence, we used an ET510/80M (Chroma Technology Corporation) emission filter (GCaMP6f) and a 630 AF50/25R (Omega optical) emission filter (tdTomato) and GaAsP photomultiplier tubes (H7422P-40 modified version without cooling; Hamamatsu Photonics). We acquired images (256 × 120 pixels or 128 × 240 pixels) at 8.01 Hz. At the end of the experiment, we acquired a z-stack of the labelled neurons to confirm the recording location.

Image processing and calculating ΔF/F

We performed all image processing and analyses using scripts written in MATLAB (MathWorks) (https://github.com/sagrawal/InterneuronAnalysis). After acquiring the images for a trial, we first applied a Gaussian filter (size 5x5 pixel, s = 3) and aligned each frame to a mean image of the trial using a sub-pixel registration algorithm (Guizar-Sicairos et al., 2008) (registered to ¼ pixel). For alignment of images, we used the red channel tdTomato fluorescence, which should not change as a function of calcium. TdTomato fluorescence remained stable over the course of each experiment (data not shown), indicating that movement artifacts were absent or small. For detecting calcium signals, we chose pixels whose mean GCaMP6f fluorescence was above a set

threshold (see Fig. 1C-H for examples). For calculating the GCaMP6f fluorescence change relative to the baseline (ΔF/F), we used the lowest average fluorescence level in a 10-frame window as the baseline fluorescence during that trial.

To investigate the velocity sensitivity of the 9Aα and 10Bα neurons (Fig. S2J-K), we first calculated the maximum slope of the ΔF/F curves for these neurons during both flexion and extension swing motions based on the frame-by-frame change in the ΔF/F value. We reasoned that the maximum slope of the ΔF/F curves more accurately represents the maximum activity level of these neurons than the maximum amplitude of the ΔF/F curves, because the calcium signal integrates the activity of the neuron over time.

CNS Electrophysiology

Cell bodies were visualized using an 850 nm IR LED (M850F2, ThorLabs) and a 40X water-immersion objective (Nikon) on a Simple Moving Microscope (SOM, Sutter Instrument). Extracellular saline was bubbled with 95% O2 / 5% CO2. The internal solution for whole-cell recordings was composed of (in mM) 140 KOH, 140 aspartic acid, 10 HEPES, 2 mM EGTA, 1 KCl, 4 MgATP, 0.5 Na3GTP, 13 neurobiotin, with pH adjusted using KOH to 7.2 and osmolality adjusted to 268 mOsm. Whole-cell patch pipettes were pulled with a P-97 linear puller (Sutter Instruments) from borosilicate glass (OD 1.5 mm, ID 0.86 mm) to have approximately 8-12 MOhm resistance. Whole-cell patch-clamp recordings were targeted to GFP-labeled cell bodies in the prothoracic region of the VNC. We used a Multiclamp 700A amplifier (Molecular Devices) for all recordings. Data were low-pass filtered at 5 kHz before they were digitized at 20 kHz by a 16 bit A/D converter (Axon Digidata 1400A, Molecular Devices Co.), and acquired in AxoScope 10.7 (Molecular Devices Co.). Stable recordings were typically maintained for 1-2 hours. Analysis of electrophysiology data was performed with custom scripts written in MATLAB (MathWorks). The liquid junction potential for the whole cell recordings was -12 mV (Gouwens and Wilson, 2009). We corrected the membrane voltages reported in the paper by post-hoc subtraction of the junction potential.

Moving the tibia/pin using a magnetic control system

We used a previously described magnetic control system (Mamiya et al., 2018) to manipulate the femur/tibia joint angle. To move the tibia/pin to different positions, we attached a rare earth magnet (1 cm height x 5 mm diameter column) to a steel post (M3x20 mm flat head machine screw) and controlled its position using a programmable servo motor (SilverMax QCI-X23C-1; Max speed 533,333 °/s, Max acceleration 83,333.33 °/s^2, Position resolution 0.045°; QuickSilver Controls). To move the magnet in a circular trajectory centered at the femur-tibia joint, we placed the motor on a micromanipulator (MP-285, Sutter Instruments) and adjusted its position while visually inspecting the movement of the magnet and the tibia using the tibia tracking camera described below. For each trial, we controlled the speed and the position of the servo motor using QuickControl software (QuickSilver Controls). During all trials, we tracked the tibia position (as described below) to confirm the tibia movement during each trial. Because it was difficult to fully flex the femur-tibia joint without the tibia/pin and the magnet colliding with the abdomen, we only flexed the joint up to ~18°. We set the acceleration of the motor to 72000 °/s^2 for all ramp and hold and swing movements. Movements of the tibia during each trial varied slightly due to several factors, including the length of the magnetic pin and the positioning of the tibia and motor.

Tracking the femur-tibia joint angle during electrophysiology and imaging experiments

To track the position of the tibia, we illuminated the tibia/pin with an 850 nm IR LED (M850F2, ThorLabs) and recorded video using an IR sensitive high-speed video camera (Basler Ace A800-510um, Basler AG) with a 1.0x InfiniStix lens (94 mm wd, Infinity). The camera used in the calcium imaging prep was further equipped with a 900 nm short pass filter (Edmund optics) to filter out the two-photon laser light. In order to synchronize the tibia movement with the recorded cell activity, the camera exposure signal was acquired at 20 kHz. To track the tibia angle, we identified the position of the painted tibia/pin against the contrasting background by thresholding the image. We then approximated the orientation of the leg as the long axis of an ellipse with the same normalized second central moments as the thresholded image (Haralick and Shapiro, 1992).

Vibrating the tibia using a piezoelectric crystal

To vibrate the tibia at high frequencies, we moved the magnet using either a piezoelectric crystal (calcium imaging prep, PA3JEW, Max displacement 1.8 μm; ThorLabs) or a preloaded piezoelectric actuator (patch-clamp electrophysiology prep, P-841.40, Physik Instrumente). To control the movement of the piezo, we generated sine waves of different frequencies in MATLAB (sampling frequency 10 kHz) and sent them to the piezo through a

single channel open-loop piezo controller (calcium imaging prep: Thorlabs; electrophysiology prep: Physik). Piezo-induced tibia movements during the calcium imaging prep were calibrated as described by Mamiya et al. (2018). Piezo-induced movements during the electrophysiology prep were calibrated using the amplitude measured by the piezo's internal sensor. For each stimulus, we presented 4 s of vibration 2-3 times with an inter-stimulus interval of 8 s. We averaged the responses within each fly before averaging across flies.

Spike detection from whole-cell recordings

To detect spikes in current clamp recordings of membrane potential, we applied the following analysis steps to our records of membrane voltage: 1) filter, 2) identify events with large peaks above a threshold, 3) compute a distance from a template for each event, 4) compute the amplitude of the voltage deflection associated with the filtered event, 5) select spikes by thresholding events based both on the distance to the filtered template (< threshold) and on the amplitude of the spike in the voltage record (> threshold). The parameter space for each of these steps was explored in an interactive spike detection interface which can be found at https://github.com/tony-azevedo/spikeDetection. Further details regarding the spike detection algorithm can be found in Azevedo et al. (2019).

Immunohistochemistry and anatomy

For confocal imaging, we crossed flies carrying the Gal4 driver to flies carrying *pJFRC7-20XUAS-IVS-mCD8::GFP* and dissected the VNC out of the thorax in *Drosophila* saline. We first fixed the VNC in a 4% paraformaldehyde PBS solution for 15 min and then rinsed the VNC in PBS three times. We next put the VNC in blocking solution (5% normal goat serum in PBS with 0.2% Triton-X) for 20 min, then incubated it with a solution of primary antibody (anti-CD8 rat antibody 1:50 concentration; anti-brp mouse for nc82 neuropil staining; 1:50 concentration) in blocking solution for 24 hours at room temperature. At the end of the first incubation, we washed the VNC with PBS with 0.2% Triton-X (PBST) three times, then incubated the VNC in a solution of secondary antibody (anti-rat-Alexa 488 1:250 concentration; anti-mouse-Alexa 633 1:250 concentration) dissolved in blocking solution for 24 hours at room temperature. Finally, we washed the VNC in PBST three times and then mounted it on a slide with Vectashield (Vector Laboratories). Following electrophysiology recordings, we dissected the VNC and brain and followed the procedure described above, but included streptavidin AlexaFluor conjugate (1:250 goat anti-mouse AlexaFluor conjugate from Invitrogen) during the secondary antibody staining to visualize neurobiotin-filled neurons. We acquired a z stack image of the slides on a confocal microscope (Zeiss 510).

Cells were traced in FIJI (Schindelin et al., 2012), using the Simple Neurite Tracing plug-in (Longair et al., 2011). For *in silico* overlay of the expression patterns of specific Gal4 lines (Figure 1I-K), we used confocal stacks of each Gal4 line with neuropil counterstaining (from the Janelia FlyLight database (Jenett et al., 2012)) and used the neuropil staining to align the expression pattern in the VNC using the Computational Morphometry Toolkit (CMTK, Jefferis et al., 2007; http://nitrc.org/projects/cmtk) to a female VNC template (Bogovic et al., 2019, Janelia Research Campus, https://www.janelia.org/open-science/jrc-2018-brain-templates).

Pharmacology

Drugs were bath applied via the saline perfusate. Tetrodotoxin (TTX, purchased from Abcam) was prepared as a concentrated stock solution in sodium citrate, picrotoxin was prepared as a concentrated stock solution in aqueous NaCl (140 mM), and methyllycaconitine citrate (MLA, purchased from Sigma-Aldrich) and atropine sulfate (Sigma-Aldritch) were prepared as stock solutions in water. Each drug was further diluted in saline for experiments for a final concentration of 1 µM (TTX and MLA), 20 µM (atropine), or 100 µM (picrotoxin). Drugs were perfused over the exposed VNC for as long as 40 minutes (MLA and atropine in the case of 13Bα and 10A cell recordings) but more often for 20 minutes. We compared cell activity before and after drug application in most cases using a Wilcoxon matched-pairs signed-rank test, except for one case in which the number of cells fell below three (Fig. S4D-E) in which case we switched to a two sample t-test.

Fly preparation for walking experiments

Fly wings were clipped under cold anesthesia (<4 mins) 24 hours before walking experiments. The fly's dorsal thorax was attached to a tungsten wire (0.1 mm diameter) with UV-curing glue (KOA 300, KEMXERT). Tethered flies were food deprived for at least 3 hours prior to being placed in the arena. In the headless preparation, the tethered flies were then decapitated under cold anesthesia and allowed to recover for 5-10 minutes prior to the experiment. Intact or headless tethered flies were positioned on a hand-milled foam treadmill ball (density: 7.3 mg/mm^3, diameter: 9.46 mm) that was suspended on a stream of air (5 l/min) and freely rotated under the fly's

movement. The ball and fly were illuminated by three IR lights (M850F2, ThorLabs) to improve motion tracking. In unloaded experiments with the headless prep, we removed the spherical treadmill, leaving the flies suspended in air. For all trials, the temperature in the chamber was maintained between 26-28 ºC with a relative humidity of 58-65%.

Tethered behavior assay

We coaxed flies to walk on the ball by displaying visual stimuli on a semi-circular green LED display (Reiser and Dickinson, 2008). To elicit forward walking, we displayed a single dark bar (width 30º) on a light background, and sinusoidally oscillated the bar at 2.7 Hz across 48.75º about the center of the fly's visual field. During periods between trials, the LED panels displayed a fixed dark stripe (30º) on a bright background in front of the tethered fly. To characterize the role of the motor neurons in behaving tethered flies, we optogenetically activated genetically targeted motor neurons. A green laser (532 nm, CST DPSS laser, Besram Technology, Inc), pulsed at 1200 Hz with a 66% duty cycle, passed through a converging lens and a pinhole (50 µm diameter) with a resulting power of 87 mW/mm^2 at the target. It was aimed at the fly's left prothoracic coxa-body wall joint, thus targeting the left T1 neuromere below the cuticle. Experiments using a driver line labeling all motor neurons (OK371-Gal4) indicated that optogenetic stimulation primarily affected neurons innervating the left prothoracic leg (Azevedo et al., 2019), though we cannot rule out effects on other VNC neurons.

For intact fly experiments, each trial was four seconds long. We presented walking flies with the visual stimulus, the flies reached a steady running speed at ~1.5 sec, and the laser stimulus began at 2 seconds. The laser stimulus randomly cycled through seven stimulus lengths: 0 ms, 30 ms, 60 ms, 90 ms, 180 ms, 360 ms, and 720 ms. For simplification, we primarily focus on a short stimulus (90 ms), a long stimulus (720 ms) and the control condition (laser omitted, 0 ms). Each fly was presented each laser stimulus six times. For headless fly experiments, we used only the longest laser stimulus length (720 ms) and the control omitted stimulus (0 ms), such that each fly had 24 laser stimulus trials (at 720 ms) and 4 control trials (no laser), randomly interleaved. Trials were separated by a 25 second period during which video data was written to disk and the LED panels displayed a fixed, stationary stripe.

Quantification of fly behavior

We used Fictrac (Moore et al., 2014) to calculate fly walking trajectories (position, speed, and rotational velocity) from live video of the spherical treadmill's rotation (Point Grey Firefly camera, imaging at 30 Hz). Trajectories were then converted from pixels to mm using the spherical treadmill's diameter of 9.46 mm. Detailed fly movements and kinematics were captured from six simultaneously triggered cameras (Basler acA800-510µm, imaging at 300 Hz) that were distributed around the fly. Digital and analog data signals were collected with a DAQ (PCIe-6321, National Instruments) sampling at 10 kHz and recorded with custom MATLAB scripts. For all experimental trials, we scored the fly's behavior in the 200 ms preceding the optogenetic stimulus as stationary, walking/turning, grooming or other. Flies that took no steps for the duration of the categorization period were classified as stationary. Flies that took at least four coordinated steps over the duration of the 200 ms period were classified as walking/turning. Trials in which the fly switched behaviors, groomed or did not display clear markers for walking/turning during the categorization period were classified as other/grooming and excluded from analyses. For each headless fly trial, both unloaded and loaded, we also scored the behavioral response to the laser stimulus during the 720 ms period following the onset of the stimulus into categories based on the repertoire of responses.

In headless fly experiments, we manually tracked the position of the left front via high-speed video during the optogenetic stimulus period. We then calculated the leg joint angles (coxa-femur, femur-tibia, and tibia-tarsus) from the position measurements. For activation experiments in 13Bα headless flies, we calculated the average change in the leg joint angles (coxa-femur, femur-tibia, tibia-tarus) over time across flies for the control (0 ms laser) and activation stimulus (720 ms laser). We calculated the change in joint angle as the difference in the average joint angle for a 200 ms period before the laser turned and the last 200 ms period of the laser activation. For activation experiments in 9Aα, we subtracted the joint angle during the frame immediately preceding laser onset from the joint angle during the frame immediately following laser offset, excluding any flies that were not stationary in the 200 ms preceding the optogenetic stimulus. We then compared this change in joint angle during trials with a 720 ms laser stimulus with trials with a 0 ms laser stimulus using bootstrap simulations with 100,000 random draws to compare changes in walking speed (Saravanan et al., 2019). We calculated the change in joint angle over time for all trials binned by initial joint position (e.g. Fig. 3E-F) to determine if the initial position of the joint affected the response to activation. Initial joint angles were determined from the camera frame before the laser stimulus started.

Comparisons across these different groups was accomplished using a 1-way ANOVA with Tukey-Kramer corrections.

For walking fly experiments (e.g. Figs. 8 and S8), we calculated the average forward velocity over time in the walking trials, for each stimulus length, for each fly. We noticed a response in the control flies (SH-Gal4) to the laser light that was correlated to the laser turning off, thus, we compared changes in speed between the control line (SH-Gal4) and each of the interneuron lines. We first calculated the change in running speed within a genotype as the average difference in speed between the 200 ms period preceding the laser stimulus and the 200 ms period occurring 200 ms after the laser onset (black brackets in Fig. 8C). We then calculated the difference between the change in running speed for each stimulus condition in the control line and the interneuron line (Fig. 8B). We then used bootstrap simulations with 100,000 random draws to compare changes in walking speed for a given motor neuron line to the control. To quantify the pausing/stopping behavior observed during activation of the 10Bα neurons, we generated a cumulative probability distribution for the first instance of freezing (speed dropping below 0.3 cm/s) within the two second period following the laser stimulus start for each walking trial (Figs. 8D and S8C).

Data and software availability

Data will be made available on the authors website (tuthill.casa) and all custom-written software will be made freely available on GitHub (https://github.com/sagrawal/InterneuronAnalysis).

Table of Genotypes

Fig. 1A	w[1118]; P{JFRC7-20XUAS-IVS-mCD8::GFP} attp40/+; iav-Gal4/+
Fig. 1C	Left: w[1118]; P{JFRC7-20XUAS-IVS-mCD8::GFP} attp40/+; P{GMR73D10-GAL4}attP2/+ Right: w[1118]/+; P{20xUAS-IVS-GCaMP6f} attP40 /+; P{GMR73D10-GAL4}attP2/P{w[+mc]=UAS-tdTomato}
Fig. 1D	Left: w[1118]; P{JFRC7-20XUAS-IVS-mCD8::GFP} attp40/+; P{GMR21D12-GAL4}attP2/+ Right: w[1118]/+; P{20xUAS-IVS-GCaMP6f} attP40; P{GMR21D12-GAL4}attP2/P{w[+mc]=UAS-tdTomato}
Fig. 1E	Left: w[1118]; P{JFRC7-20XUAS-IVS-mCD8::GFP} attp40/+; P{GMR64C04-GAL4}attP2/+ Right: w[1118]/+; P{20xUAS-IVS-GCaMP6f} attP40 /+; P{GMR64C04-GAL4}attP2/P{w[+mc]=UAS-tdTomato}
Fig. 1F	Left: w[1118]; P{JFRC7-20XUAS-IVS-mCD8::GFP} attp40/ P{28A12-p65.AD} attp40; P{VT000606-GAL4.DBD}attP2/+ Right: w[1118]; P{20xUAS-IVS-GCaMP6f} attP40 / P{28A12-p65.AD} attp40; P{ VT000606-GAL4.DBD }attP2/ P{w[+mc]=UAS-tdTomato}
Fig. 1G	Left: w[1118]; P{JFRC7-20XUAS-IVS-mCD8::GFP} attp40/ P{52E12-p65.AD} attp40; P{ VT044946-GAL4.DBD}attP2/+ Right: w[1118]; P{20xUAS-IVS-GCaMP6f} attP40 / P{52E12-p65.AD} attp40; P{VT044946 -GAL4.DBD}attP2/ P{w[+mc]=UAS-tdTomato}
Fig. 1H	Left: w[1118]; P{JFRC7-20XUAS-IVS-mCD8::GFP} attp40/ P{ VT043132-p65.AD} attp40; P{VT045623-GAL4.DBD}attP2/+ Right: w[1118]; P{20xUAS-IVS-GCaMP6f} attP40 / P{VT043132 -p65.AD} attp40; P{VT045623-GAL4.DBD}attP2/ P{w[+mc]=UAS-tdTomato}
Figs. 2, S2	Recordings obtained from two different lines: w[1118]; P{JFRC7-20XUAS-IVS-mCD8::GFP} attp40/ P{28A12-p65.AD} attp40; P{VT000606-GAL4.DBD}attP2/+ w[1118]; P{JFRC7-20XUAS-IVS-mCD8::GFP} attp40/ +; P{25G05-GAL4}attP2/+
Figs. 3, S3	w[1118]; P{28A12-p65.AD} attp40/+; P{VT000606-GAL4.DBD}attP2/ P{y[+t7.7] w[+mC]=20XUAS-IVS-CsChrimson.mVenus}attP2
Figs. 4-5, S4-5	w[1118]; P{JFRC7-20XUAS-IVS-mCD8::GFP} attp40/ P{52E12-p65.AD} attp40; P{VT044946-GAL4.DBD}attP2/+

Fig. 6	w[1118]; P{52E12-p65.AD} attp40/+; P{VT044946-GAL4.DBD}attP2/ P{y[+t7.7] w[+mC]=20XUAS-IVS-CsChrimson.mVenus}attP2
Figs. 7, S7	w[1118]; P{JFRC7-20XUAS-IVS-mCD8::GFP} attp40/ P{VT043132-p65.AD} attp40; P{VT045623-GAL4.DBD}attP2/+
Fig. 8	Control (SH-Gal4): w[1118]; P{10A07-p65.AD} attp40/+; P{y[+t7.7] w[+mC]=20XUAS-IVS-CsChrimson.mVenus}attP2/+ 10Bα-Gal4: w[1118]; P{VT043132-p65.AD} attp40/+; P{VT045623-GAL4.DBD}attP2/ P{y[+t7.7] w[+mC]=20XUAS-IVS-CsChrimson.mVenus}attP2 13Bα-Gal4: w[1118]; P{28A12-p65.AD} attp40/+; P{VT000606-GAL4.DBD}attP2/ P{y[+t7.7] w[+mC]=20XUAS-IVS-CsChrimson.mVenus}attP2 9Aα-Gal4: w[1118]; P{52E12-p65.AD} attp40/+; P{VT044946-GAL4.DBD}attP2/ P{y[+t7.7] w[+mC]=20XUAS-IVS-CsChrimson.mVenus}attP2
Fig. S1A	w[1118]; P{JFRC7-20XUAS-IVS-mCD8::GFP} attp40/ P{28A12-p65.AD} attp40; P{VT000606-GAL4.DBD}attP2/+
Fig. S1B	w[1118]; P{JFRC7-20XUAS-IVS-mCD8::GFP} attp40/ P{28A12-p65.AD} attp40; P{VT000606-GAL4.DBD}attP2/+
Fig. S1C	w[1118]; P{JFRC7-20XUAS-IVS-mCD8::GFP} attp40/ P{ VT043132-p65.AD} attp40; P{VT045623-GAL4.DBD}attP2/+
Fig. S1D-F	w[1118]; P{20xUAS-IVS-GCaMP6f} attP40 / P{28A12-p65.AD} attp40; P{ VT000606-GAL4.DBD }attP2/ P{w[+mc]=UAS-tdTomato}
Fig. S1G-I	w[1118]; P{20xUAS-IVS-GCaMP6f} attP40 / P{52E12-p65.AD} attp40; P{VT044946 -GAL4.DBD}attP2/ P{w[+mc]=UAS-tdTomato}
Fig. S1J-L	w[1118]; P{20xUAS-IVS-GCaMP6f} attP40 / P{VT043132 -p65.AD} attp40; P{VT045623-GAL4.DBD}attP2/ P{w[+mc]=UAS-tdTomato}
Fig. S6	w[1118]; P{VT014013-p65.AD} attp40/+; P{30A10-GAL4.DBD }attP2/ P{y[+t7.7] w[+mC]=20XUAS-IVS-CsChrimson.mVenus}attP2
Fig. S8A	Control (SH-Gal4): w[1118]; P{10A07-p65.AD} attp40/+; P{y[+t7.7] w[+mC]=20XUAS-IVS-CsChrimson.mVenus}attP2/+ 10Bα-Gal4: w[1118]; P{VT043132-p65.AD} attp40/+; P{VT045623-GAL4.DBD}attP2/ P{y[+t7.7] w[+mC]=20XUAS-IVS-CsChrimson.mVenus}attP2
Fig. S8B-C	13Bα-Gal4: w[1118]; P{28A12-p65.AD} attp40/+; P{VT000606-GAL4.DBD}attP2/ P{y[+t7.7] w[+mC]=20XUAS-IVS-CsChrimson.mVenus}attP2 9Aα-Gal4: w[1118]; P{52E12-p65.AD} attp40/+; P{VT044946-GAL4.DBD}attP2/ P{y[+t7.7] w[+mC]=20XUAS-IVS-CsChrimson.mVenus}attP2 9Aα2-Gal4: w[1118]; P{VT014013-p65.AD} attp40/+; P{30A10-GAL4.DBD }attP2/ P{y[+t7.7] w[+mC]=20XUAS-IVS-CsChrimson.mVenus}attP2

Supplemental Videos

Video S1. Optogenetic activation of 13Bα neurons in headless flies. Related to Figure 3. The video shows the movements of the fly's left front leg caused by optogenetic activation of 13Bα neurons in headless flies with legs either unloaded or loaded. The video shows 1) the leg movement during the entire 720 ms laser stimulation period slowed 5X; 2) several examples from different trials with different flies slowed 5X.

Video S2. Optogenetic activation of 9Aα neurons in headless flies. Related to Figure 6. The video shows the movements of the fly's left front leg caused by optogenetic activation of 9Aα neurons in headless flies with legs either unloaded or loaded. The video shows the leg movement during the entire 720 ms laser stimulation period slowed 5X.

Video S3. Optogenetic activation of 10Bα neurons in walking flies. Related to Figure 8. The video shows walking flies pausing during optogenetic activation of 10Bα neurons. The video shows 1) A single fly's behavior during 720ms of laser stimulation slowed 5X; 2) several example trials during 720ms of laser stimulation slowed 5X.

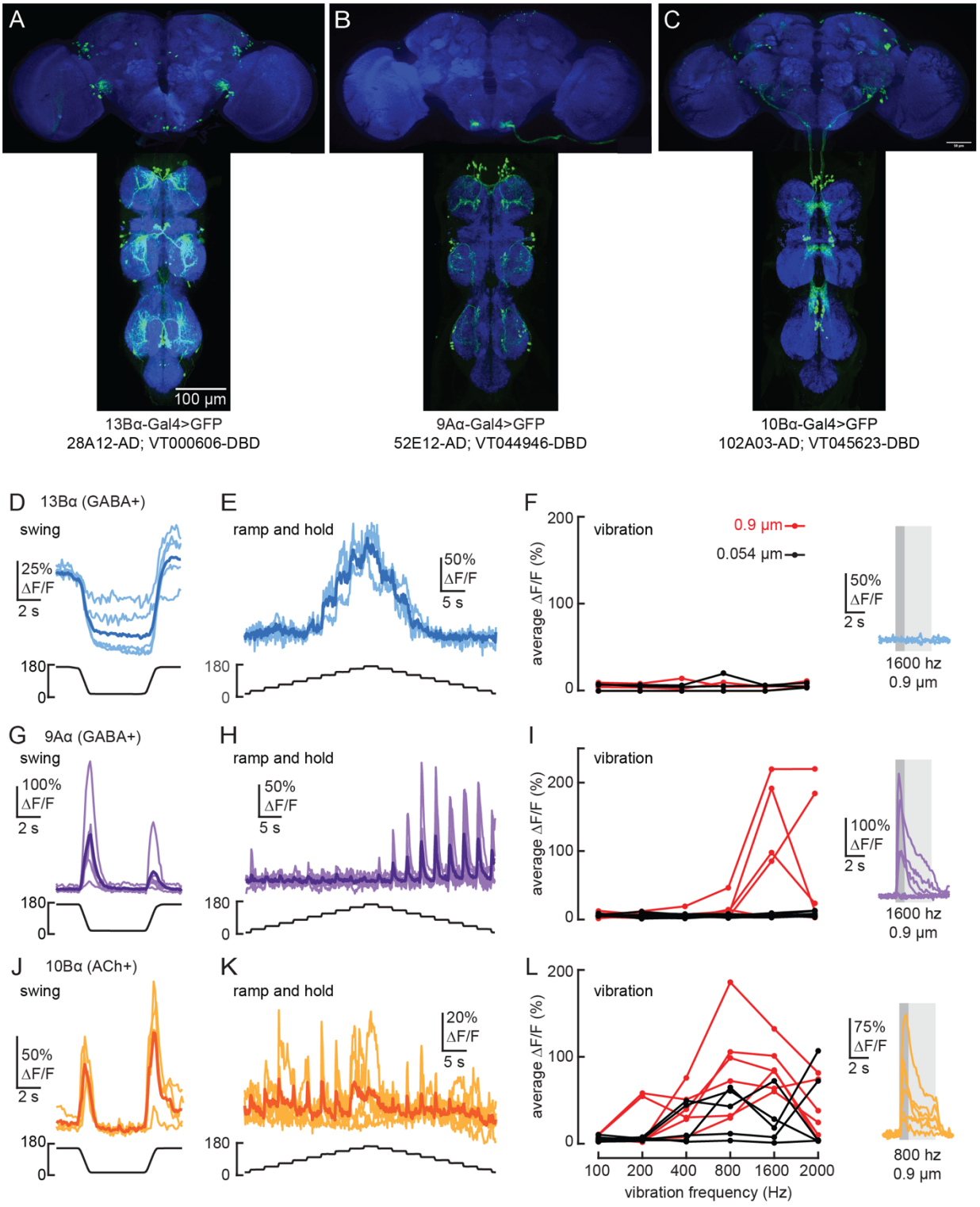

Figure S1. Transformation of leg proprioceptive signals by 13Bα, 9Aα, and 10Bα cells in the fly VNC. A-C) VNC and brain expression of the split-Gal4 lines predominantly used to label each cell-type. Blue: neuropil stain (nc82), Green: GFP. D-E) Calcium signals from 13Bα neurons during tibia swing (D, n = 5) or ramp-and-hold (E, n = 3). The thicker line shows the response average F) Left: 13Bα activity during vibration stimuli. Each line represents an average response from one fly to three stimulus repetitions. Right: Calcium signals from 13Bα cells during a 1600 Hz, 0.9 µm amplitude vibration. The light-gray box indicates when the vibration was applied, and the dark-gray box indicates the window of activity averaged for the left plot. G-H) Calcium signals from 9Aα during tibia swing (G, n = 6) or ramp-and-hold (H, n = 7). I) Left: 9Aα activity during vibration stimuli. Right: Calcium signals from 9Aα cells during a 1600 Hz, 0.9 µm amplitude vibration. J-K) Calcium signals from 10Bα neurons during tibia swing (J, n = 4) or ramp-and-hold (K, n = 5). L) Left: 10Bα activity during vibration stimuli. Right: Calcium signals during an 800 Hz, 0.9 µm amplitude vibration.

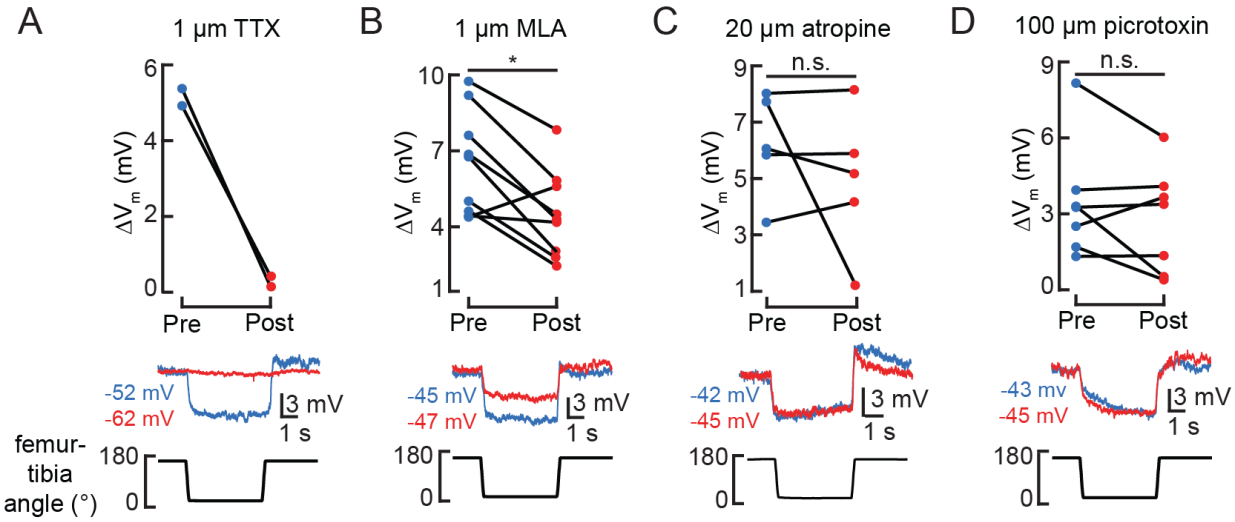

Figure S2. Pharmacological manipulation of synaptic inputs to 13Bα neurons. A-D) Top: the change in membrane potential after the femur is flexed before (blue) and after (red) drug application. Each line is the response of a single cell (*p<0.05; n.s.: not significant, Wilcoxon matched-pairs signed-rank test). Example membrane potential traces before (blue) and after (red) drug application are shown below.

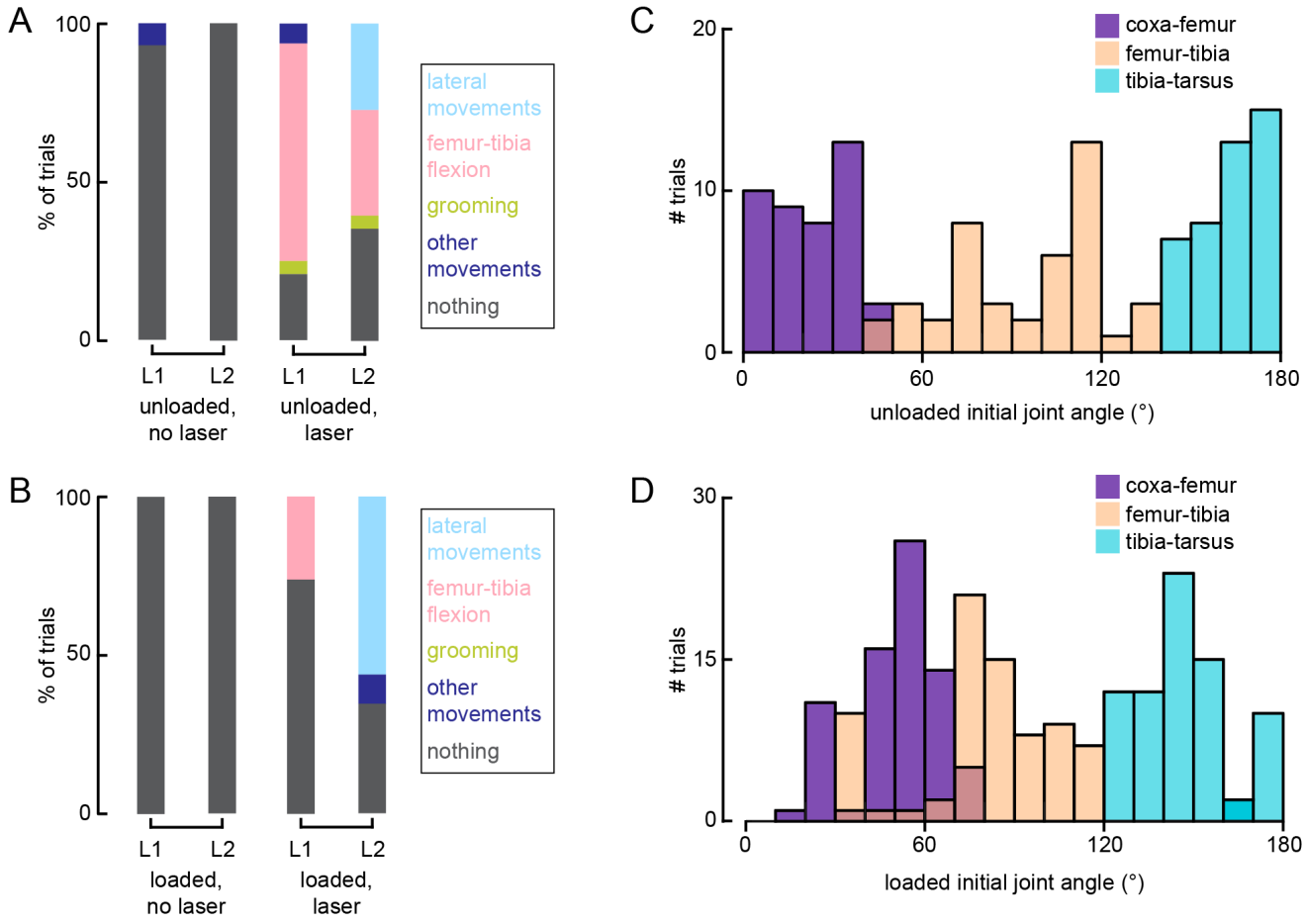

Figure S3. Optogenetic activation of 13Bα neurons causes movement of the L1 and L2 legs.
A-B) Distribution of observed behaviors after the laser turned on when flies were either unloaded (A, No laser: n = 11 trials; Laser: 44 trials) or loaded (B, No laser: n = 26 trials; Laser: n = 74 trials). L1: front left leg; L2: middle left leg C-D) Distribution of initial joint angles for all trials when flies were either unloaded (C, n = 50 trials) or loaded (D, n = 100 trials).

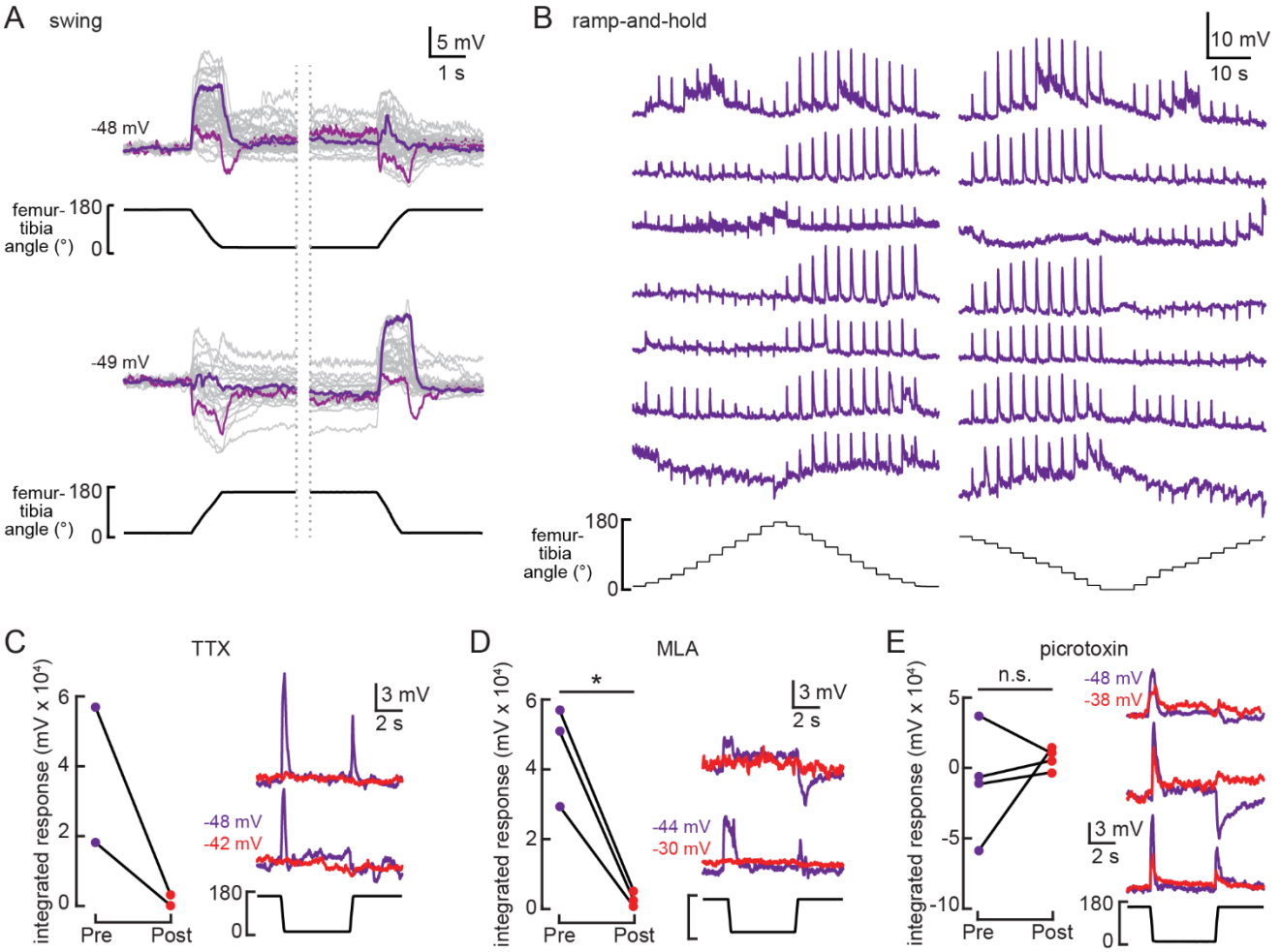

Figure S4. 9Aα cells are a heterogenous population of neurons that encode tibial flexion.
A) Whole-cell current clamp recordings from 9Aα neurons during tibia swing movements. Each trace is the averaged response to three stimulus repetitions. Example traces are highlighted in purple and magenta (top: n = 35, bottom: n = 24). B) Examples 9Aα responses during ramp-and-hold stimuli. Each row of traces is a recording from an individual cell. C-E) Left: 9Aα recordings during swing movements before (purple) and after (red) drug application. Graphs plot the integrated change in membrane potential (*p<0.05; n.s.: not significant, two sample t-test). Right: example traces before (purple) and after (red) drug application.

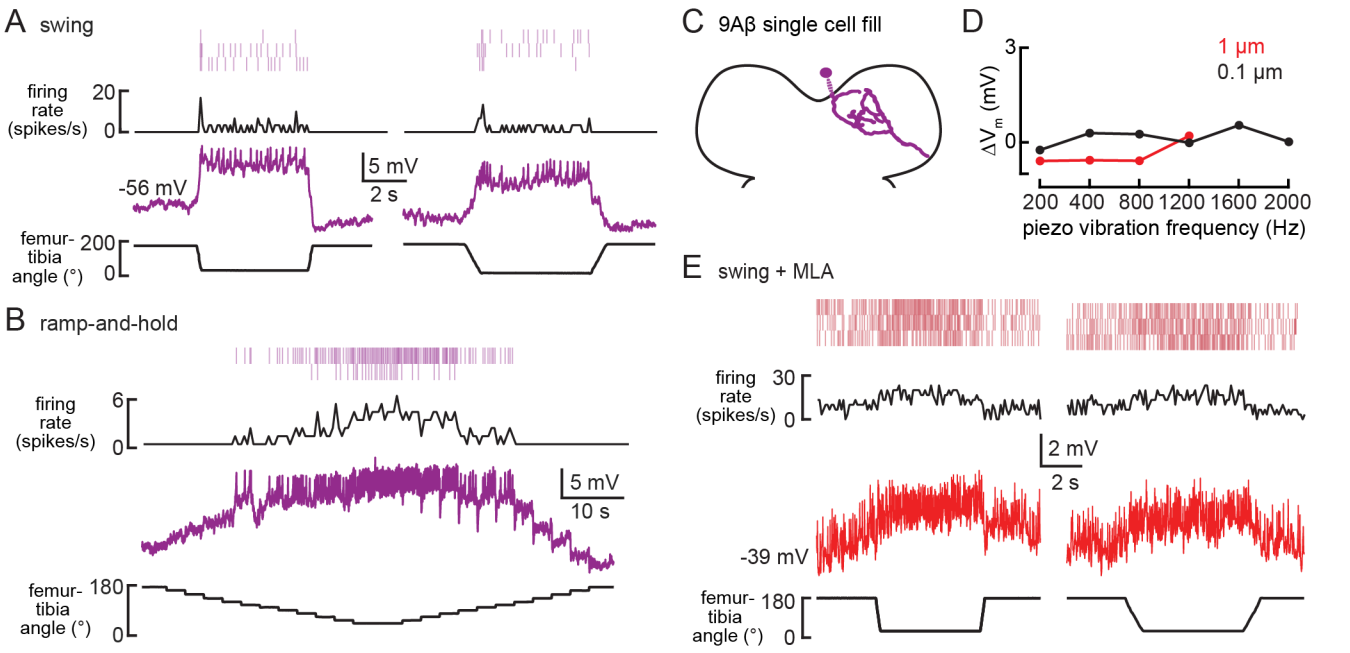

Figure S5. 9Aβ encodes flexed tibia positions. A-B) Whole-cell current clamp recordings from a 9Aβ neuron during the indicated swing (A) or ramp-and-hold (B) movements of the femur-tibia joint. Average firing rate and spike rasters are shown above. C) Morphology of a 9Aβ neuron reconstructed after filling with Neurobiotin. D) The change in membrane potential during the first 500 ms after vibration stimulus onset. E) Activity recorded from a 9Aβ during tibia swing after application of an antagonist of nicotinic acetylcholine receptors, MLA (1 µM). Average firing rate and spike rasters are shown above.

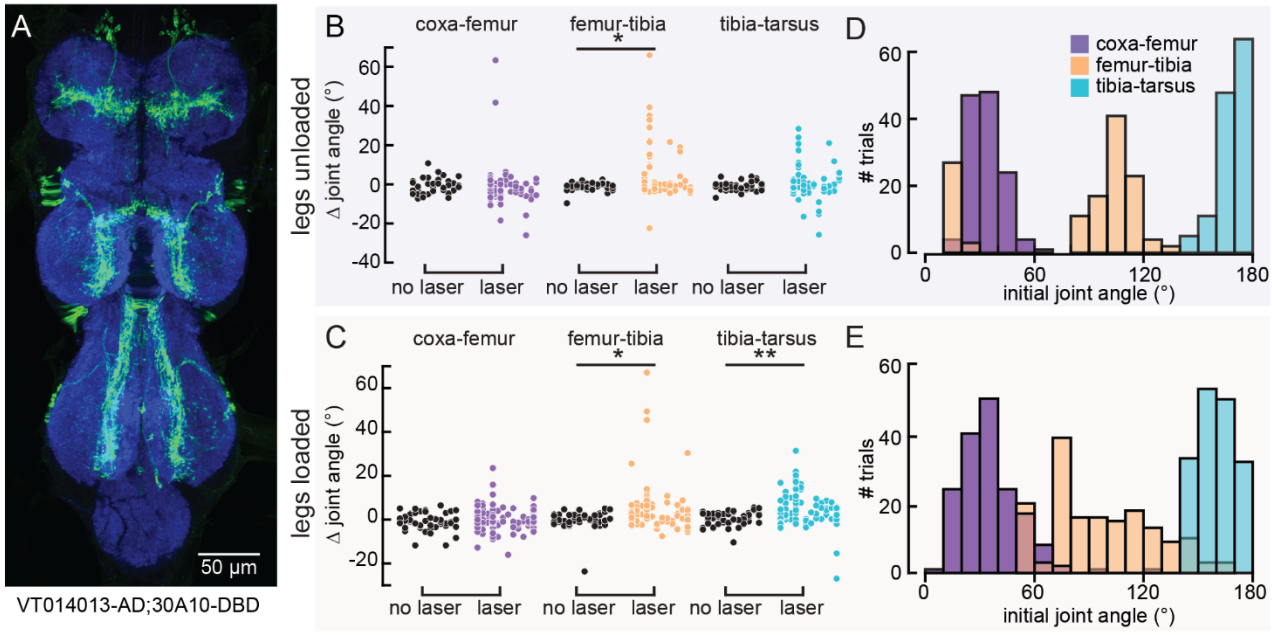

Figure S6. Optogenetic activation of 9Aα neurons using another split-Gal4 line causes a similar extension of the femur-tibia and tibia-tarsus. A) VNC expression of 9Aα2-Gal4. Blue: neuropil stain (nc82), Green: GFP. B-C) Change in joint angle after 720 ms during trials in which the laser was on (purple, orange, and blue data points) or off (black data points). Each column is data from a single fly. We expressed CsChrimson in 9Aα neurons using 9Aα2-Gal4. The fly was either unloaded (B, n = 10 flies) or loaded (C, n = 12 flies). (*p<0.05, **p<0.005, bootstrapping with false discovery rate correction). D-E) Distribution of initial joint angles of 9Aα2-Gal4>CsChrimson flies before the start of the 720 ms stimulus period when flies were either unloaded (D, n = 128 trials) or loaded (E, n = 168 trials).

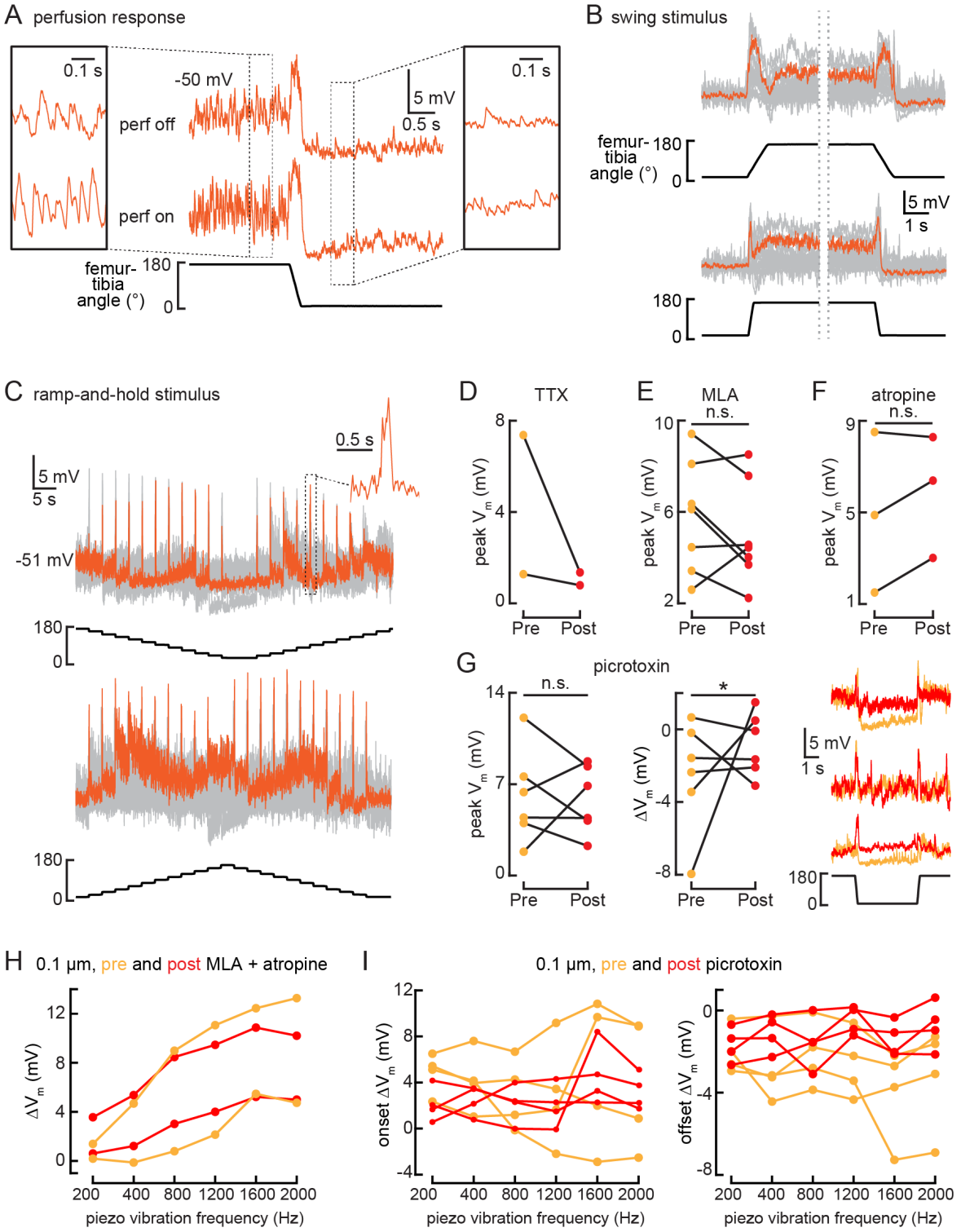

Figure S7. 10Bα cells encode bidirectional tibia movements and tibia vibration. A) Example whole-cell recording from a 10Bα neuron when the tibia was flexed. Saline perfusion was either absent ("off," top row) or present ("on," bottom row). Insets show an expanded view of the cell's response when the tibia was extended (left) or flexed (right). When the tibia is extended, vibrations from the saline perfusion cause increased oscillations in the membrane potential. These oscillations disappear when the tibia is flexed. B-C) 10Bα recordings during swing (B) or ramp-and-hold (C) movements of the femur-tibia joint. An example response is highlighted in orange (B: n = 24; C: top: n = 16, bottom: n = 24). D-F) The peak membrane potential while the femur is flexed before (orange) and after (red) drug application (*p<0.05; n.s.: not significant, Wilcoxon matched-pairs signed-rank test). G) Left: the peak membrane potential while the femur is flexed before (orange) and after (red) application of the GABAa and GluCl antagonist, picrotoxin (100 µM). Middle: the change in membrane potential after tibia flexion before (orange) and after (red) application of picrotoxin (n.s.: not significant, *p>0.05, Wilcoxon matched-pairs signed-rank test). Right: example traces before (orange) and after (red) application of picrotoxin. H-I) The change in membrane potential during the first 500 ms after vibration onset before (orange) and after (red) drug application.

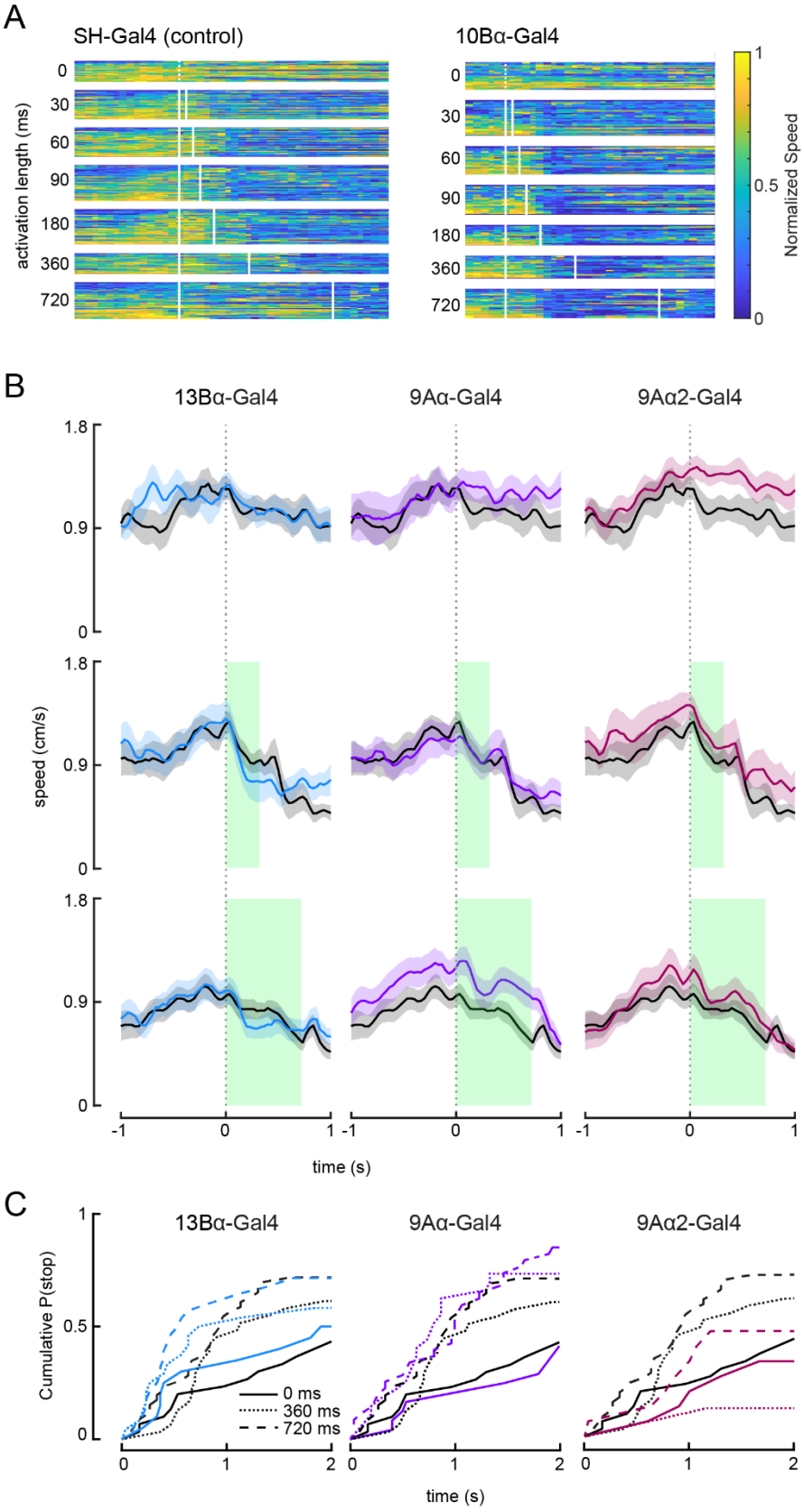

Figure S8. Optogenetic activation of 10Bα neurons causes flies to freeze and stop walking. A) Heat maps indicating fly's forward velocity across different genotypes and laser stimulations. Each row is data from a single trial, and velocity has been normalized by dividing by the maximum speed per trial. White boxes indicate when the laser was on. B) Average treadmill forward velocity (+/- SEM) of walking flies during no laser trials (top row) or trials with a 360 ms (middle row) or 720 ms (bottom row) laser stimulus. Green boxes indicate the duration of optogenetic stimulation. C) Cumulative probability of a fly stopping (velocity <0.3 cm/s) during trials with no laser or trials with a 360 ms or 720 ms laser stimulus.